Controls on Mg isotopic fractionation between deep mantle phases and relict signatures of a terrestrial magma ocean

A. M. Walker, Remco C. Hin and Tim Elliott

Addresses: Department of Earth Sciences, University of Oxford, South Parks Road, Oxford, OX1 3AN, UK, Institute of Environmental Geology and Geoengineering, Consiglio Nazionale delle Ricerche, Via Bianco Mario 9, 20131, Milano MI, Italy and School of Earth Sciences, University of Bristol, Wills Memorial Building, Queen's Road, Bristol, BS8 1RJ, UK. email: andrew.walker@earth.ox.ac.uk

This manuscript will be submitted to Geochimica et Cosmochimica Acta

Controls on Mg isotopic fractionation between deep mantle phases and relict signatures of a terrestrial magma ocean

Andrew M. Walker[a,*], Remco C. Hin[b], Tim Elliott[c]

[a] *Department of Earth Sciences, University of Oxford, South Parks Road, Oxford, OX1 3AN, UK*
[b] *Institute of Environmental Geology and Geoengineering, Consiglio Nazionale delle Ricerche, Via Bianco Mario 9, 20131, Milano MI, Italy*
[c] *School of Earth Sciences, University of Bristol, Wills Memorial Building, Queen's Road, Bristol, BS8 1RJ, UK*

Abstract

We use density functional theory to investigate the fractionation of Mg isotopes between phases in the lower mantle. Our results support previous work and show that coordination number plays an important role in controlling isotopic fractionation, with bridgmanite (perovskite-structured $MgSiO_3$) preferentially incorporating lighter Mg isotopes into its highly coordinated site compared to periclase (MgO). A trade-off between pressure (which enhances fractionation) and temperature (which reduces it) allows this preference to be evident across all lower mantle conditions explored, even to the high temperatures of the chondritic liquidus (e.g. $\Delta^{26/24}Mg_{Per-Bdm}$ is 0.04‰ at 4200 K and 87 GPa). In additional numerical experiments we separate the effect of coordination number from differences in bond length between different phases and these allow us to build an ionic model which parameterises magnesium

*Corresponding author
Email address: andrew.walker@earth.ox.ac.uk (Andrew M. Walker)

isotope fractionation as a function of bond length, coordination number, and temperature. This model provides us with a preliminary means to describe isotope partitioning between solid and liquid phases when making predictions of Mg isotopic differences generated during terrestrial magma ocean crystallisation. We find that Mg isotopic fractionation between bridgmanite and melt, at lower mantle conditions, is sufficient to generate detectable differences in the Mg isotopic compositions of a residual melt or solid cumulate phase, relative to bulk Earth. More specifically, we show that isolation of a reservoir of cumulate bridgmanite that is some 3-15 percent by mass of the mantle could account for the super-chondritic $^{26}Mg/^{24}Mg$ of accessible terrestrial peridotite samples. Long-standing problems remain in physically retaining such a reservoir at the core mantle boundary over Earth history, but our results help quantify possible tests of such a scenario.

Keywords: Mg isotopes, density functional theory, ionic model, coordination number, magma ocean

---

1. Introduction

Study of mass-dependent isotopic variations has traditionally been the domain of low temperature geochemists, since the magnitudes of such fractionations are inversely proportional to temperature squared (Urey, 1947) and so most evident at the Earth's surface. However, realisation of the opportunity afforded by MC-ICPMS to make isotopic measurements of a wide range of elements to significantly better than 100 ppm makes this discipline of increasing interest for the study of high-temperature processes (e.g. Young et al., 2015; Soderman et al., 2022; Wang et al., 2023). Although small, iso-

topic differences generated in the Earth's interior are now typically amenable to analysis.

A likely important factor in the magnitude of mass-dependent isotopic fractionations in the deep Earth is the effect of pressure. Whilst the high temperatures of the planet's interior act against mass-dependent isotopic variability, associated increases in pressure and the resulting changes in the coordination number and bond length of common mineral sites can act to promote isotopic fractionation. The work of Huang et al. (2013, 2014) and Wu et al. (2015) examined the interplay of these counter-acting continuous and discontinuous changes with depth for the major elements Mg and Si. Here we take some further steps in this direction by making a first principles exploration of the isotopic fractionation of magnesium between mantle phases over a wide range of appropriate pressures and temperatures. In particular, we wish to estimate fractionation factors for key phases, at a range of lower mantle conditions to assess Mg isotopic fractionations that may be associated with magma ocean crystallisation.

Magnesium is an attractive target because it is a high-abundance, stoichiometric constituent of several major mantle phases, that occurs in only one oxidation state. There is also a comparatively large (8%) relative mass difference between its two major isotopes, which is an important contributing factor in the generation of discernible isotopic fractionation.

Mg isotopic differences inferred to result from equilibrium partitioning between co-existing, shallow mantle minerals have been reported for more than a decade (e.g. Young et al., 2009). Such observations, supported by theoretical analysis (Young et al., 2009; Schauble, 2011; Huang et al., 2013),

have led to a useful rule of thumb that the isotopic composition of an element in a more highly coordinated lattice site is lighter than in a site with lower coordination. In this general context, it is significant that high pressure phases hosting Mg show a range of coordination numbers from 6-fold in periclase (Per: rock salt structured MgO) to 8–12 in bridgmanite (Bdm: perovskite-structured $MgSiO_3$; Yagi et al., 1978). The high coordination state of Bdm, the most abundant silicate mineral in the Earth, relative to co-existing phases is of particular interest. Wu et al. (2015) considered the effect of coordination number increases associated with phase changes in the transition zone including calculations on Bdm in the uppermost lower mantle (to 24.5 GPa). However, 'ionic' models of isotope fractionation focus on bond length variation rather than coordination number as an important controlling parameter (Young et al., 2009, 2015; Sossi and O'Neill, 2017; Blanchard et al., 2017). We thus supplement our study of mantle phases with numerical experiments designed to separate the effect of coordination number and bond length on isotope fractionation in a series of hypothetical oxide structured materials.

Whilst it is of interest to understand mineral-mineral fractionations (Huang et al., 2013; Wu et al., 2015), ultimately it is of broader geological significance to constrain mineral-melt fractionations, which might drive larger scale isotopic differences in the Earth. For example, if crystallization of a magma ocean involves phases that fractionate Mg isotopes, global Mg isotopic heterogeneities may be generated by mineral-melt segregation. Despite progress with models of aqueous solutions (Rustad and Bylaska, 2006; Kowalski and Jahn, 2011; Kowalski et al., 2013; Gao et al., 2018; Wang et al., 2019), and

more recent work on isotope fractionation in basaltic melts at low pressure (Rabin et al., 2023) determinations of melt-mineral isotopic fractionations remains challenging for first principles calculations (see Blanchard et al., 2017, for a review of these methods). To circumvent this problem, previous studies invoked the apparent lack of Mg isotopic fractionation between olivine and mafic melt at low pressure, inferred from the absence of systematic variability in the Mg isotopic compositions of a suite of magmas controlled by addition and loss of olivine (Teng et al., 2007), to support the use of forsterite (Mg_2SiO_4: Fo) as a proxy for melt in their numerical experiments (Wu et al., 2015).

Our treatment of the melt phase in this contribution is different in two respects. Firstly, as a low pressure datum we use a recent, high-precision, direct determination of the isotopic fractionation factor for Mg between olivine and melt (Liu et al., 2022), which is discernibly less than unity. Secondly, we use our experiments with different hypothetical phases with fixed MgO composition, but different Mg coordination environments and variable Mg-O bond lengths to produce a parameterised model of Mg isotope fractionation. We argue that this approach has predictive power for phases, such as melt, where only the atomic structure is known. Pinned by the new determination of the fractionation factor between forsterite and melt at low pressure, we then use this model, in combination with knowledge of how melt structure changes with pressure (Karki et al., 2006; de Koker, 2009) to calculate Mg isotope fractionation between mantle minerals and coexisting melts in a crystallising deep magma ocean. Although rudimentary, this is the first attempt to quantify the influence of pressure on melt structure in modelling isotopic

fractionations during the crystallisation of magma oceans.

2. Methods

In order to explore the effect of pressure, temperature and crystal chemistry on the fractionation of ^{24}Mg from ^{26}Mg we employed a first-principles atomic-scale approach to calculate the reduced partition functions for the two isotopes in Fo, Per, Bdm and five hypothetical MgO polymorphs. While not directly addressing the fractionation with a high pressure melt phase, we argue below that these calculations are sufficient to give the sense of the fractionation behaviour when extrapolated from the known behaviour at low pressure to extreme conditions not easily amenable to experiment. Our approach to these calculations follows a number of previous studies (e.g. Blanchard et al., 2009; Javoy et al., 2012; Li and Liu, 2011; Li et al., 2009; Méheut et al., 2007, 2009; Rustad and Dixon, 2009) including examples of the fractionation of Mg isotopes (Young et al., 2009; Schauble, 2011; Huang et al., 2013; Wu et al., 2015; Wang et al., 2017; Duan et al., 2023; Wang et al., 2023), which have established the predictive accuracy of first principles simulation to address isotopic fractionation. However, we believe our calculations are the first to consider conditions relevant to the crystallisation of a global magma ocean.

Key to the calculations is the definition of the reduced partition function, $\beta(X, Y, Y^\star)$, which is the equilibrium constant for the exchange reaction for two isotopes of an element (Y and $Y^\star$) between the material of interest, X, and an ideal gas (Bigeleisen and Mayer, 1947; Urey, 1947). The equilibrium fractionation factor, $\alpha(X^1, X^2, Y, Y^\star)$, between two crystalline phases (X^1

and X^2) is then given by the ratio of the reduced partition functions or, more conveniently, as a difference in the expected measured isotopic content:

$$\begin{aligned}\Delta Y^{\star}_{X^1-X^2} &\approx 1000\ln\left(\alpha(X^1,X^2,Y,Y^{\star})\right)\\ &= 1000\ln\left(\beta(X^1,Y,Y^{\star})\right)-1000\ln\left(\beta(X^2,Y,Y^{\star})\right),\end{aligned}\qquad(1)$$

where inclusion of the factors of 1000 means that $\Delta Y^{\star}_{X^1-X^2}$ is the ‰ difference between the two phases. The important feature of this approach is that, for crystals and in the harmonic approximation, $\beta(X,Y,Y^{\star})$ can be calculated from knowledge of only the phonon density of states (Keiffer, 1982; Schauble, 2004):

$$\beta(X,Y,Y^{\star})=\prod_{i=1}^{N_q}\left[\prod_{j=1}^{3N_{\rm at}}\left(\frac{\omega^{\star}_{i,j}}{\omega_{i,j}}\frac{e^{-h\omega^{\star}_{i,j}/(2kT)}}{1-e^{-h\omega^{\star}_{i,j}/(kT)}}\frac{1-e^{-h\omega_{i,j}/(kT)}}{e^{-h\omega_{i,j}/(2kT)}}\right)\right]^{w_i},\qquad(2)$$

where $\omega_{i,j}$ and $\omega^{\star}_{i,j}$ are the phonon frequencies at the $i^{\rm th}$ reciprocal lattice sampling point for the $j^{\rm th}$ branch in crystal X containing the Y and $Y^{\star}$ isotopes, respectively, T is the absolute temperature, k is the Boltzmann constant and h is the Plank constant. For a simulation cell containing $N_{\rm at}$ atoms, the products run over the $3N_{\rm at}$ modes for each of the N_q points sampled in the first Brillouin zone (the three acoustic modes at the Γ point representing translations of the crystal are excluded from the product). The Brillouin zone is sampled using the scheme due to Monkhorst and Pack (1976). Symmetry of the reciprocal lattice is used to avoid the wasteful calculation of frequencies for equivalent points with weighting factors, w_i, being applied to properly account for points on the edge of the sampled irreducible volume. The computational task is thus to calculate $\omega_{i,j}$ and $\omega^{\star}_{i,j}$ with sufficient accuracy to lower mantle pressure.

We calculate phonon frequencies using density functional perturbation theory (DFPT: Baroni et al., 1987, 2001) as implemented in the CASTEP code (Clark et al., 2005) using the plane-wave and pseudopotentials approach (Payne et al., 1992). First, density functional theory (DFT: Hohenberg and Kohn, 1964; Kohn and Sham, 1965) is used to determine the crystal structure (atomic positions and cell parameters) of each crystal at target pressures in 10 GPa increments between -10 and 140 GPa. We adopt the generalised gradient approximation (GGA) of Perdew et al. (1996) and make use of norm-conserving pseudopotentials for nuclei and core electrons (only 3s and 3p, 2p, and 3s electrons are explicitly included for Si, O, and Mg atoms, respectively). Explicit valence electrons are expanded on a plane wave basis with a cut-off energy of 900 eV for all three phases and with the electronic band structure sampled on 3×3×3, 4×2×4 and 4×4×4 Monkhorst-Pack grids for Bdm, Fo and Per, respectively (these parameters were chosen by testing for convergence of the phonon frequencies, but reproduce the crystal structures as described below).

Once the equilibrium crystal structure is determined, the phonon frequencies are given by the square root of the eigenvalues of the dynamical matrix:

$$D^{\kappa\kappa'}_{\alpha\alpha'}(\mathbf{q})\varepsilon_{j\kappa,\alpha\mathbf{q}} = \omega^2_{\mathbf{q},j}\varepsilon_{j\kappa,\alpha\mathbf{q}}, \tag{3}$$

which is, in turn, a function of the second derivatives of the energy of the system with respect to atomic displacements:

$$D^{\kappa\kappa'}_{\alpha\alpha'}(\mathbf{q}) = \frac{1}{\sqrt{m_\kappa m_{\kappa'}}} \sum_a \left(\frac{\partial^2 E}{\partial \mathbf{u}_{\kappa,\alpha} \partial \mathbf{u}_{\kappa',\alpha'}} \right) e^{-i\mathbf{q}.\mathbf{R}_a}, \tag{4}$$

where E is the internal energy of the system, m_κ and $\mathbf{u}_{\kappa,\alpha}$ is the mass and

displacement of atom κ in direction α, $\mathbf{q}$ is the wave vector, and the summation runs over the distances, $\mathbf{R}_a$, between periodic replicas of the two atoms. The eigenvectors, ε, in Equation 3 describe how the atoms move for each phonon frequency. These lattice dynamics calculations are performed using variational DFPT (Gonze, 1997; Gonze and Lee, 1997) using the implementation described by Refson et al. (2006). An important point is that E does not depend on the masses of the atoms in the crystal. This property can be used to minimise the number of DFPT calculations needed to evaluate the reduced partition function by storing the matrix of second derivatives and reusing this for both isotopic substitutions. The 'phonons' utility, distributed with CASTEP, allows this optimisation alongside Fourier interpolation (Giannozzi et al., 1991), which allows phonon frequencies to be estimated at wave vectors between those included in the DFPT calculation. We note that under all the conditions we consider the DFPT calculations yield real eigenvalues for all phases indicating that they are dynamically (but not necessarily thermodynamically) stable.

Our calculations of isotope fractionation in hypothetical MgO polymorphs are designed to allow us to explore the relative importance of local bonding environment (bond length and coordination number) and chemistry on the equilibrium fractionation of Mg isotopes. We thus performed DFT and DFPT calculations on a range of prototypical 'MX' structures with fixed MgO composition and with the Mg atom occupying different coordination sites. In each case we first optimised the crystal structure while constraining symmetry at 0 GPa before building a super-cell, calculating the dynamical matrix, and evaluating the reduced partition coefficients following the ap-

proach outlined above. For these calculations we considered five structures in addition to periclase: the cubic and hexagonal ZnS structures, the NiAs structure and its 'inverse', and the primitive cubic CsCl structure. Many of these MgO polymorphs have small unit cells. When calculating the change in vibration behaviour due to the substitution of ^{26}Mg for ^{24}Mg, we attempt to keep the distance between substituted sites the same. To do this we use the conventional cubic unit cell for the rock salt structure, a 2×2×2 supercell for the CsCl structure and 2×2×1 supercells for the NiAs and ZnS structures. In order to probe the relationship between bond length and Mg isotope fractionation we also scaled the lattice vectors after optimisation, increasing or decreasing their length as needed to set the bond length before calculation of the dynamical matrix. While this results in structures with negative or very high fictive pressures, it means that the bond lengths for different structures and coordination numbers overlapped enabling us to decouple the effect of bond length from that of coordination number.

3. Results

The primary aim of our DFPT calculations is to establish the phonon frequencies across the irreducible wedge of the Brillouin zone for the three phases at pressures between −10 and 140 GPa in order to allow the calculation of the reduced partition functions. Our strategy for choosing the electronic parameters of the calculations that need to be converged (k-point sampling and plane wave cut-off) was to increase these until the frequency of the Γ point optic modes changed by less than 0.5 cm^{-1}. This also gives suitably converged lattice parameters (Table 1) and atomic positions. As

expected given the use of a GGA functional, these values are larger than the experimentally determined cell parameters. This makes little difference to the calculated reduced partition functions. Comparison with results from the local-density approximation, which underestimates the cell parameters, shows that the calculated reduced partition functions are not strongly modified by choice of functional. Convergence of the numerical parameters in the calculation is a more important effect.

Table 1: Calculated lattice parameters of forsterite, periclase and bridgmanite as a function of pressure from static lattice minimisation. A parametrisation of the volume with temperature and pressure derived from lattice dynamics and DFPT can be found in the SI.

Phase and lattice parameter	0 GPa	25 GPa	50 GPa	120 GPa
Per, a (Å)	4.25	4.08	3.97	3.77
Fo, a (Å)	4.80	4.64	4.55	4.41
Fo, b (Å)	10.32	9.67	9.27	8.48
Fo, c (Å)	6.05	5.73	5.55	5.27
Bdm, a (Å)	4.83	4.68	4.56	4.33
Bdm, b (Å)	4.98	4.85	4.76	4.60
Bdm, c (Å)	6.97	6.75	6.60	6.31

The number of reciprocal space sampling points in Equation 2, the 'q-point sampling', must also be sufficiently large to allow the calculated reduced partition functions to converge. For periclase we find that sampling only the Γ point results in an underestimate of $1000 \ln\left(\beta(\mathrm{Per}, {}^{24}\mathrm{Mg}, {}^{26}\mathrm{Mg})\right)$ relative to the fully converged case by almost 2 ‰ at 300 K even if Fourier interpolation is used to add a dense grid of additional points. Sampling on a 3×3×3

Monkhorst-Pack grid gives convergence better than 0.1‰ and interpolating onto a 7×7×7 grid better than 0.01 ‰ convergence at 300 K. This behaviour mirrors that reported by Schauble (2011) and we perform a similar convergence analysis to calculate reduced partition functions for the three phases such that, at the temperatures of interest, results are fully converged.

A further adjustable parameter which appears to have received less attention is the separation of adjacent substituted isotopes in the periodic models. As pointed out by Méheut et al. (2007), Equation 2 is derived under the assumption that isotopic substitutions are in the dilute limit where the free energy change associated with a substitution on a particular site does not depend on the separation between the site and its periodic images. We investigated the convergence of the reduced partition function with increasing separation in periclase as shown in Table 2. We find that convergence for this material is rather slow and, for the range of simulation cell sizes probed, that there may still be an error of ∼0.1 ‰ at 300K. Unfortunately, the computational cost of the DFPT calculations grows very quickly as the separation between isotope images grows and this prevents a more detailed analysis of this source of error for any of the phases considered here. However, given the simulation cells used in our calculations (a 2×2×2 primitive super cell for periclase with a 4×4×4 q-point sampling and the conventional orthorhombic cells for forsterite and bridgmanite with 3×1×3 and 3×3×3 q-point sampling, respectively) we believe that all our calculations are converged to much better than 0.01 ‰ at temperatures above 1000 K.

We express the temperature dependence of the reduced partition functions by fitting the computed values to a convenient polynomial equation

Table 2: Convergence in calculated reduced partition function, $1000 \ln\left(\beta(\mathrm{MgO}, {}^{24}\mathrm{Mg}, {}^{26}\mathrm{Mg})\right)$, at 300 K in periclase with increasing separation between adjacent isotopically substituted magnesium atoms.

Mg* – Mg* separation (Å)	Reduced partition function (‰)	Simulation cell	Fraction of Mg atoms substituted
3.01	25.76	primitive	100%
4.25	27.67	conventional	25 %
6.02	26.13	$2 \times 2 \times 2$ primitive	12.5 %
8.51	26.38	$2 \times 2 \times 2$ conventional	3.125 %

also used by Schauble (2011) and Huang et al. (2013):

$$1000 \ln\left(\beta(T)\right) = AT^{-6} + BT^{-4} + CT^{-2}, \tag{5}$$

where A, B and C are fitted constants given for the three phases at each pressure in Table 3. We compare our results with those of Schauble (2011), Huang et al. (2013) and Wu et al. (2015) in Figure 1 and, overall, find good agreement with previous work. In particular, all results for forsterite are consistent and this is despite the differences in the choice of exchange-correlation functional (we use a GGA while most previous work makes use of the local-density approximation). The very non-linear behaviour of the results from Huang et al. (2013) below 400 K is because these workers only parametrise their model using results at higher temperatures. Similarly, the more linear behaviour of the results of Wu et al. (2015) is because these authors fit to a lower order polynomial than that used here. Given the excellent agreement for forsterite, explaining the somewhat larger difference between the results of recent studies of Per and Bdm is not trivial. For Per some of the difference

can be attributed to the separation of periodic images of the isotopic substitution. This convergence is not smooth (see Table 2) but the 1.3 ‰ difference at 300 K for changing the separation from 4.25 Å to 8.51 Å would explain a large portion of the discrepancy. A more general source of the difference can be attributed to the different choice of exchange-correlation functional. This would imply that this has a more important role for Bdm than Per or Fo, but the reason why this would be the case is not obvious. Nevertheless, given the differences in the details of the methodology, the agreement between the different studies is remarkable, and at least indicates that geochemical predictions derived from these calculations have value where experiments have not been carried out. Figure 1 also shows the effect of pressure on the reduced partition functions. In all cases, and in common with the results of Wu et al. (2015), pressure acts to increase the calculated reduced partition function and thus counteract the effect of temperature. We show how these changes with temperature and pressure interact to give variations in the expected equilibrium isotopic fractionation in Figure 2 where the variations in $1000 \ln\left(\alpha(\mathrm{Per}, \mathrm{Fo}, {}^{24}\mathrm{Mg}, {}^{26}\mathrm{Mg})\right)$ and $1000 \ln\left(\alpha(\mathrm{Bdm}, \mathrm{Fo}, {}^{24}\mathrm{Mg}, {}^{26}\mathrm{Mg})\right)$ are shown.

Table 3: Fitted constants for Equation 5 giving a parameterisation of $1000 \ln\left(\beta(X, {}^{24}\mathrm{Mg}, {}^{26}\mathrm{Mg})\right)$ as a function of temperature in the harmonic approximation for crystal cell parameters optimised at different applied pressures.

	A (K^6)	B (K^4)	C (K^2)
Per, 0 GPa	1.3325×10^{14}	-1.4605×10^{10}	2.4985×10^{6}
Per, 25 GPa	2.8276×10^{14}	-2.7247×10^{10}	3.6338×10^{6}
Per, 50 GPa	5.3100×10^{14}	-4.3427×10^{10}	4.6299×10^{6}
Per, 120 GPa	2.0417×10^{15}	-1.1163×10^{11}	7.0470×10^{6}
Fo, 0 GPa	1.8414×10^{14}	-1.6279×10^{10}	2.4312×10^{6}
Fo, 25 GPa	4.9086×10^{14}	-3.6942×10^{10}	3.7982×10^{6}
Fo, 50 GPa	9.6399×10^{14}	-6.2194×10^{10}	4.9505×10^{6}
Fo, 120 GPa	3.0675×10^{15}	-1.5004×10^{11}	7.7714×10^{6}
Bdm, 0 GPa	2.0352×10^{14}	-1.6193×10^{10}	2.2502×10^{6}
Bdm, 25 GPa	3.8318×10^{14}	-2.7832×10^{10}	3.1142×10^{6}
Bdm, 50 GPa	6.4226×10^{14}	-4.2223×10^{10}	3.9157×10^{6}
Bdm, 120 GPa	1.7920×10^{15}	-9.4452×10^{10}	5.9946×10^{6}

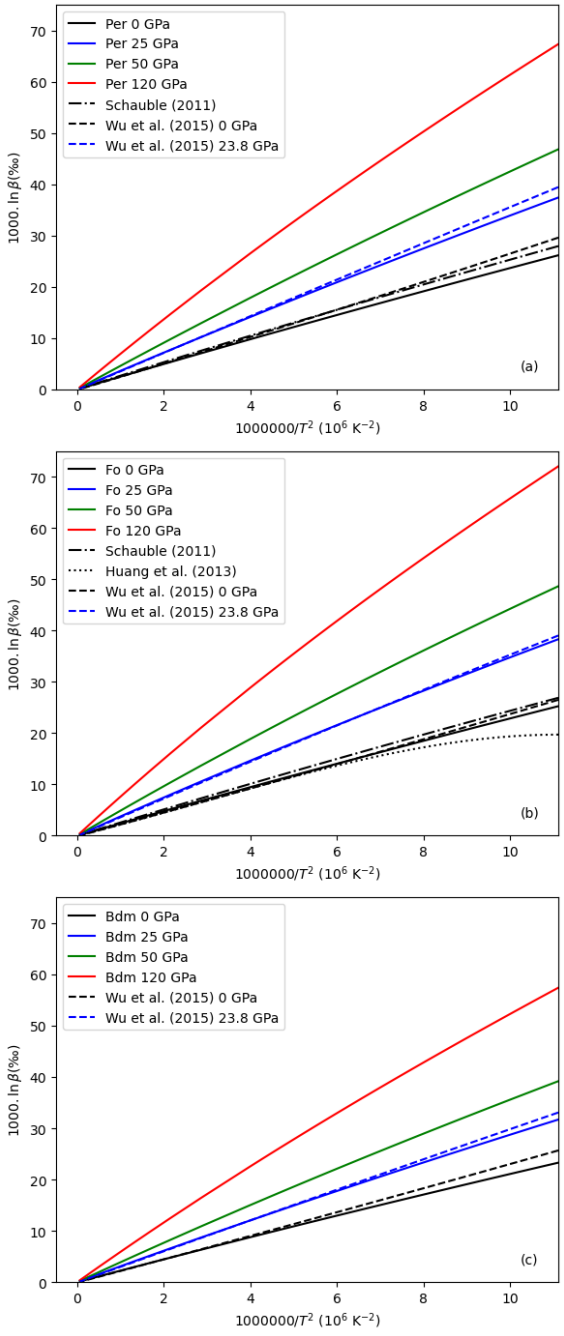

Figure 1: Calculated reduced partition functions for (a) periclase, (b) forsterite and (c) bridgmanite as a function of temperature at pressures of 0 (black), 25 (blue), 50 (green) and 120 (red) GPa. In all cases this increases with increasing pressure and decreasing temperature. Previously published results are also shown using the same colour scale for comparison. Schauble (2011): dot-dashed lines; Huang et al. (2013): dotted line; Wu et al. (2015): dashed lines (showing results at 0 and 23.8 GPa).

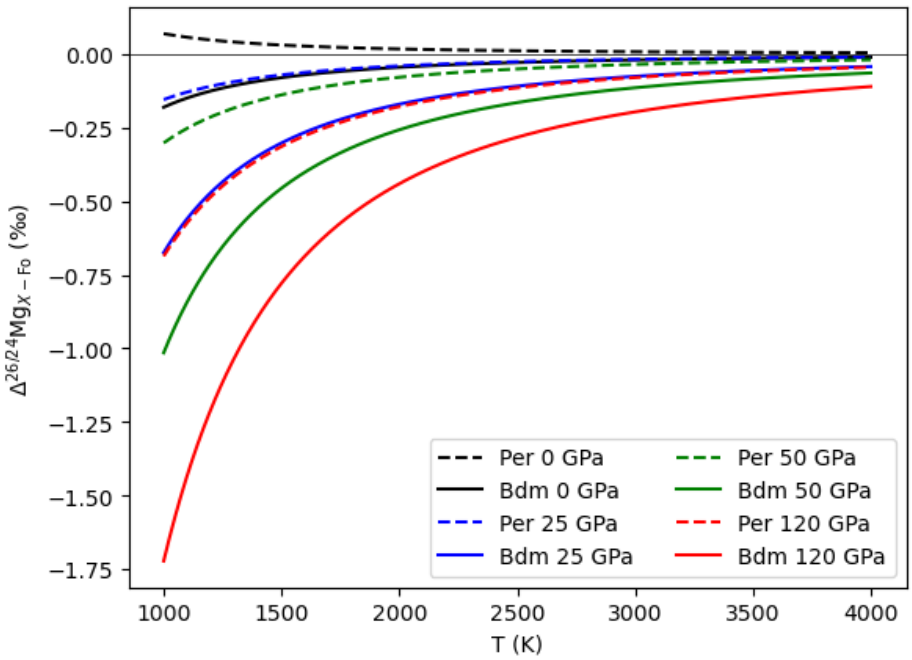

Figure 2: Calculated equilibrium partitioning between forsterite and bridgmanite (solid lines) or periclase (dashed lines) as a function of temperature and cell volume for fixed sized simulation cells corresponding to static lattice optimisation (i.e. at 0 K, and neglecting the zero-point energy) at 0 (black), 25 (blue), 50 (green) and 120 (red) GPa.

3.1. Structural controls on isotope fractionation

The equilibrium fractionation factor between Fo (or Per) and Bdm indicates that Bdm will always tend to preferentially incorporate isotopically lighter Mg when in equilibrium with the phases with six coordinate Mg. At 0 GPa and 1000 K this effect, if fully expressed, should result in a measurable relative difference of $^{26}Mg/^{24}Mg$ between Fo and Bdm ($\Delta^{26/24}Mg_{Fo-Bdm}$) of nearly 0.2 ‰. Increasing temperature rapidly reduces the fractionation but increasing pressure counteracts this effect: at 50 GPa $\Delta^{26/24}Mg_{Fo-Bdm}$ is greater than 0.2 ‰ to about 2500 K. The predicted fractionation between Per and Fo is considerably smaller. At 0 GPa the lighter Mg isotopes are predicted to be preferentially incorporated into Per but pressure reverses this trend with the heavier isotopes preferred by Fo at 25 and 50 GPa. At all pressures the expected fractionation between the two six coordinate phases is smaller than that between the six coordinated phases and the more highly coordinated Bdm. This strong effect of Mg coordination number is reminiscent of the results of Huang et al. (2013), who found that phases with six coordinate Mg (forsterite, diopside and enstatite) only weakly differentiate between ^{24}Mg and ^{26}Mg, but that these phases become enriched in the heavier Mg isotopes compared to pyrope and majorite garnet, both with eight coordinate Mg. In common with our results, Huang et al. (2013) and Wu et al. (2015) also found that increasing pressure acts to increase this fractionation between phases with different Mg coordination number, an effect that can be explained by the different compressibility of sites with different coordination. This is in contrast to the case of silicon in which there is little influence of pressure in isotopic fractionation between mantle phases (Huang

et al., 2014). However, these changes in coordination number are accompanied by changes in bond length, which are expected to alter the vibrational frequencies and thus isotope fractionation. It is unclear from our results on mantle phases whether coordination number or bond length is the dominant structural control on Mg isotope fractionation and we performed numerical experiments using hypothetical MgO polymorphs designed to resolve this.

We consider Mg in six different structural environments. In the cubic and hexagonal ZnS structures Mg is tetrahedrally coordinated with an Mg – O bond length of about 2.0 Å. The difference between these structures is in the stacking of layers of tetrahedra which means the structures have different second coordination shells around the isotopically substituted Mg. In the rock salt (Per) and NiAs structures Mg sits within six coordinated sites with Mg – O bond lengths of about 2.1 Å. The octahedra in Per share corners while octahedra in the NiAs structure share faces and edges. The NiAs structure has a second site where Mg is in trigonal prismatic coordination. In this structure all edges are shared. Finally, in the primitive cubic CsCl structure Mg is eight coordinated with with Mg – O bond lengths of about 2.3 Å and with all faces shared between adjacent polyhedra. Key structural parameters at 0 GPa and the calculated reduced partition functions for these structures are given in Table 4.

We parameterise the effect of temperature on the reduced partition functions of the six MX structures in the same way as we treated the results for mantle phases presented above. Parameters of these fits are shown in Table 5 with the reduced partition functions shown in Figure 3. It appears from inspection of Table 4 and Figure 3 that the structure of the first coor-

Table 4: Summary parameters of hypothetical MgO crystal structures showing controls on $1000 \ln\left(\beta(X, {}^{24}\mathrm{Mg}, {}^{26}\mathrm{Mg})\right)$ at 300 K

	Mg coordination number	Mg – O bond lengths (Å)	$Mg^\star$ – $Mg^\star$ separation (Å)	300 K reduced partition function (‰)
hexagonal ZnS structure	[4]	1.995	5.134	30.14
cubic ZnS structure	[4]	2.000	5.641	30.05
NaCl structure (periclase)	[6]	2.127	6.017	26.13
NiAs structure (octahedral)	[6]	2.140	5.158	26.06
NiAs structure (trigonal prismatic)	[6]	2.153	5.233	23.18
CsCl structure	[8]	2.302	5.317	18.12

dination shell explains almost all of the variability in partitioning between these simple hypothetical structures with identical chemistry. At least for these systems, the nature of the second coordination shell, and the sharing of corners, edges and faces between coordination polyhedra is relatively unimportant. However, this analysis does not account for the variability in bond lengths between structures with different coordination number at the same pressure.

Table 5: Fitted constants for Equation 5 giving a parameterisation of $1000 \ln\left(\beta(X, {}^{24}\mathrm{Mg}, {}^{26}\mathrm{Mg})\right)$ as a function of temperature in the harmonic approximation for hypothetical MgO crystal structures optimised at 0 GPa.

	A (K^6)	B (K^4)	C (K^2)
hexagonal ZnS structure	2.2580×10^{14}	-2.1812×10^{10}	2.9271×10^{6}
cubic ZnS structure	2.2551×10^{14}	-2.1729×10^{10}	2.9183×10^{6}
NaCl structure (periclase)	1.3325×10^{14}	-1.4605×10^{10}	2.4985×10^{6}
NiAs structure (octahedral)	1.5567×10^{14}	-1.6076×10^{10}	2.5052×10^{6}
NiAs structure (trigonal prismatic)	9.9342×10^{13}	-1.1700×10^{10}	2.2039×10^{6}
CsCl structure	9.3173×10^{13}	-1.0320×10^{10}	1.7341×10^{6}

To distinguish between true coordination effects and the effect of different bond lengths we vary these independently by scaling the lattice vectors of five of the hypothetical MgO polymorphs (omitting the hexagonal ZnS structure as it is so similar to the cubic ZnS structure). This allows us to calculate the reduced partition function for different bond lengths in otherwise identical structures as shown in Figure 4. In this analysis structures with low coordination number and large bond lengths correspond to situations with negative pressure while small bond lengths for structures with high coordination num-

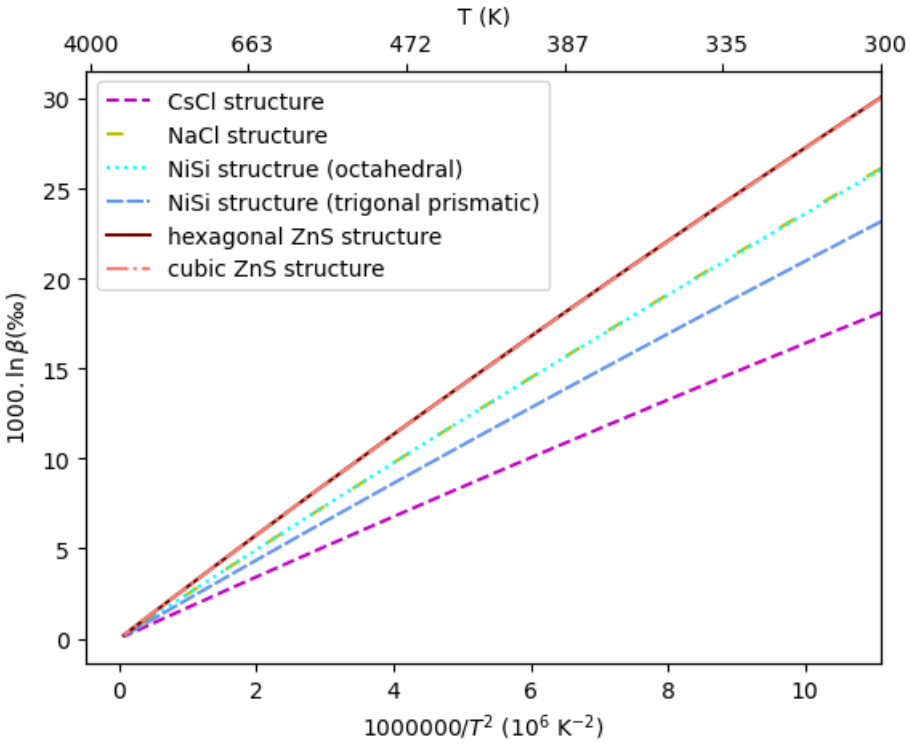

Figure 3: Calculated reduced partition functions for various MX structures with fixed MgO composition (see text for discussion). In common with the silicates, structures with low Mg coordination number (e.g. the ZnS structures with four coordinate Mg shown in overlapping red colours) consistently show a larger value of β than structures with high Mg coordination number (e.g. the eight coordinate CsCl structure, shown in purple). Values of β for structures with Mg in octahedral coordination (greens) or other six coordinate Mg environments (blue) fall between these upper and lower values.

bers correspond to situations with positive pressure (e.g. the largest bond length for cubic ZnS in Figure 4 corresponds to a pressure of −20.6 GPa and the smallest bond length for the CsCl structure corresponds to a pressure of 86.7 GPa).

Results of these calculations show a clearly separated effect of both bond length and coordination number on the reduced partition function. A reduction in bond length for a given coordination number increases the reduced partition function. In contrast, reducing the coordination number for a given bond length decreases the reduced partition function. For a given pressure increasing the coordination number increases the bond length and this effect can be significant. For example, the highlighted data points corresponding to the 0 GPa bond lengths show a decrease in reduced partition function with increasing coordination number. This effectively reverses the direct effect of bond length. In contrast to the clear effect of bond length and coordination number, we see little evidence of mineral chemistry playing a significant role for Mg isotope fractionation: our results for bridgmanite and forsterite closely follow the trends established by the MgO polymorphs with the same coordination numbers. We note that the trend shown in Figure 4 shows a similar general trend to that found for Ca by Xiao et al. (2022) but that our results for Mg show none of the mixing between structures with different coordination numbers and less scatter than Xiao et al.'s results for Ca. This is likely to be due to the different coordinating anions (O, F, S and P) and wider range structures, including solid solutions, in Xiao et al.'s dataset.

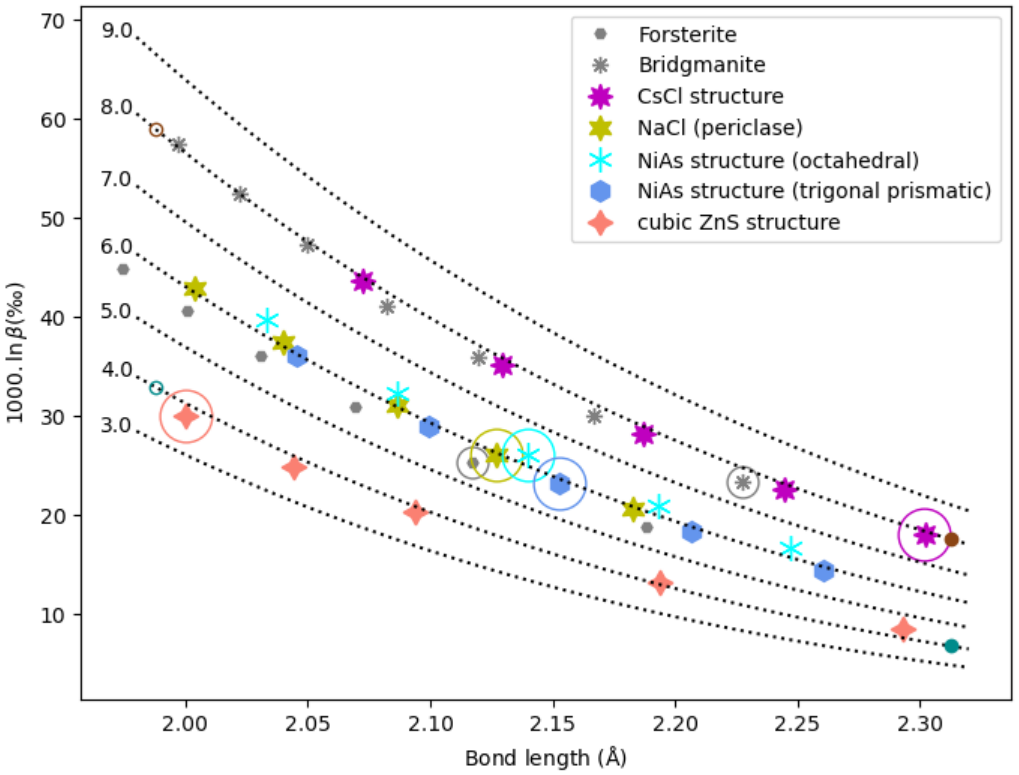

Figure 4: Large symbols: reduced partition functions at 300 K for a range of MX structured material with composition MgO. Number of sides or points on each symbol indicates the coordination number and the large circles mark the bond length at 0 GPa. Grey symbols: forsterite (-10 to 50 GPa) and bridgmanite (0 to 120 GPa). Dotted lines show the predictions of the fitted model. Small filled and unfilled circles show the models illustrated in Figure 8

3.2. The effect of thermal expansion on isotope fractionation

For all the results described so far we have neglected the effect of thermal expansion on phonon frequencies and thus on isotopic fractionation. To investigate the importance of this we must go beyond the harmonic approximation and consider the differential thermal expansion of the phases. This effect is most naturally captured using the statically constrained quasi-harmonic approximation (e.g. Wentzcovitch et al., 2010), because this can make use of the same DFPT calculations performed to evaluate the isotopic fractionation. Similarly to Wang et al. (2023), for each cell volume, V, (found by performing variable cell geometry optimisation with an applied pressure but neglecting the effect of temperature) we calculate the phonon frequencies and use these to evaluate the Helmholtz free energy. As described in the SI, the resulting volume – energy data is used to fit isothermal third-order Birch–Murnaghan equations of state (EOS) with the temperature dependence of the EOS parameters defined by fifth order polynomials. Because pressure is the derivative of the Helmholtz free energy with respect to volume, we can use these equations of state to evaluate the cell volume as a function of temperature and pressure (Figure 5).

We also evaluated β as a function of temperature at each cell volume and fit this data to a polynomial in volume and temperature (polynomial coefficients are tabulated in the SI). In order to evaluate the equilibrium fractionation factor as a function of pressure and temperature (for example, along a geotherm) we first evaluate the cell volume for each phase, then evaluate β at that volume and temperature for each of the phases. In common with previous results (e.g. Wang et al., 2023) the inclusion of thermal expansion

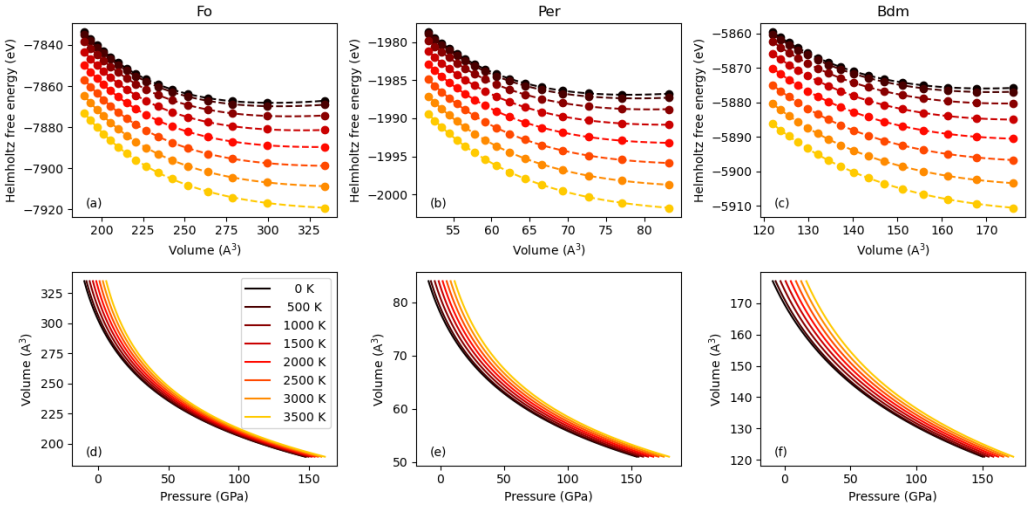

Figure 5: Isothermal third-order Birch–Murnaghan equations of state (dashed lines) fitted to lattice dynamics calculations of energy as a function of cell volume (circles) for Fo (a), MgO (b), and Bdm (c) at eight temperatures. These are used to give the cell volume as a function of pressure and temperature (d – f) and incorporate thermal expansivity into our models.

always reduces our estimate of β. However, conditions in a global magma ocean involve large compression and high temperatures such that fractionation between phases will depend on the balance of relative compressibility and thermal expansion. This is shown in Figure 6 where we compare results from the evaluation of Equation 1 using the quasi-harmonic approach with the results derived by neglecting thermal expansion at different depths in the Earth. We have used the chondritic liquidus of Andrault et al. (2011) as our geotherm. This choice, while not representing the likely conditions with depth in the Earth at any point in time, gives a maximum temperature for equilibration, and thus a lower bound on the fractionation factor between the three phases. Even at the relatively high temperatures considered here the difference between Bdm and the six coordinate phases is still significant. The correction due to differential thermal expansion is rather small but is potentially important (up to $\sim$0.02 ‰) with, for this choice of geotherm, a maximum in the fractionation factor between Fo and Bdm $>$ 0.1 ‰ at depths corresponding to the upper part of the lower mantle.

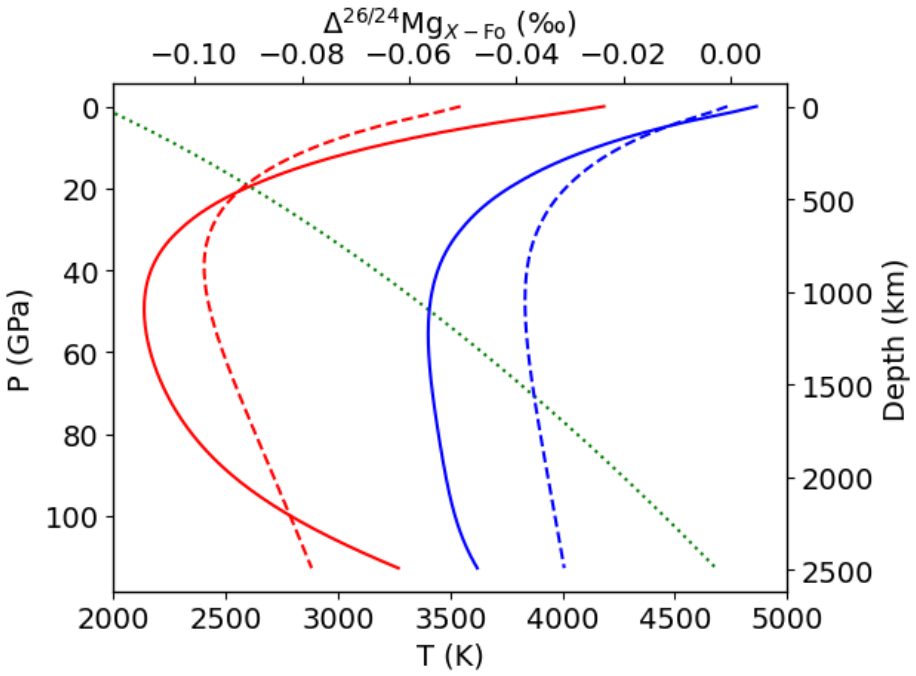

Figure 6: Calculated equilibrium partitioning (top axis) between forsterite and bridgmanite (red lines) or periclase (blue lines) as a function of depth (right axis) along a chondritic liquidus. Dashed lines neglect thermal expansion. The green doted line relates depth to pressure (left axis) and temperature (bottom axis) for the chondritic liquidus.

4. Discussion

Our calculations have shown that equilibration between solid Bdm and either Per or Fo leads to a mass-dependent fractionation of ^{24}Mg from ^{26}Mg and that this effect is significant to temperatures extending well into the lower mantle. This equilibrium fractionation is caused by differences in coordination altering the equilibrium bond lengths in the phases and this coupled effect outweighs the direct variation in fractionation caused by the change in coordination alone. Overall this results in 8–12 coordinated Mg in Bdm becoming relatively enriched in the lighter Mg isotopes compared to 6 coordinated Mg in Per or Fo. The coupled effect of coordination and bond length on fractionation leads to the possibility of fractionation of Mg isotopes between Bdm and a coexisting melt phase during crystallisation of a global magma ocean if Mg in the melt has a different coordination and/or bond length than Mg in Bdm.

The structure and properties of silicate liquids have been the subject of study using density functional theory combined with molecular dynamics (e.g. Stixrude and Karki, 2005). These simulations allow the bond length and coordination of Mg in silicate melts under the temperature, pressure and chemical conditions relevant to a global magma ocean to be determined. In pure liquid MgO, the average Mg coordination number is found to be 4.5–5 at low pressure. This increases with increasing pressure reaching about 6 at 60 GPa and 7 above 150 GPa (Karki et al., 2006). In liquid silicates, Mg coordination number depends on composition and is between 4 and 6 at low pressure and increases with increasing pressure. For example, in liquid $MgSiO_4$ at 4000 K the coordination number is around 5 with a bond length

of around 1.96 Å at 0 GPa and this changes to a coordination number of 6.5 with a bond length of around 1.92 Å at 60 GPa (de Koker et al., 2009). In $CaMgSi_2O_6$ the coordination number is higher, around 6 at 0 GPa increasing to ∼7.5 by 60 GPa (Sun et al., 2011). In general the coordination number tends to decrease slightly with decreasing temperature or with the addition of hydrogen, but both effects become less important at pressures above about 20 GPa (Mookherjee et al., 2008). Overall, at depths > 700 km we expect Mg silicate liquids in a crystallising magma ocean to have lower coordination number and shorter bond lengths than that in the coexisting liquidus phase, which is Bdm. In order to make semi-quantitative predictions of this fractionation we parameterise the mean Mg–O bond lengths and Mg coordination numbers for liquid Mg_2SiO_4 reported in de Koker et al. (2009) and shown in Figure 7. We then use these as input for an 'ionic model' and predict the reduced partition function for Mg in the melt as described below.

4.1. An ionic model of fractionation in silicate melts

Even with average structural information of the melt in hand, quantifying the isotopic fractionation between crystals and liquid in a cooling magma ocean is not trivial because of the lack of both appropriate empirical data and DFT simulations investigating isotope fractionation in liquids. However, as we detail below, we can estimate the crystal-liquid fractionation using empirical data for olivine-liquid fractionation of Mg isotopes at atmospheric pressure and a first order model of the pressure effect on the force constant of Mg-O bonds in ultramafic silicate liquid. Liu et al. (2022) have recently shown empirically that $^{26}Mg/^{24}Mg$ ratios in olivine (Fo_{82}) are 0.071‰ lower than in the glass of the basaltic lavas they crystallised from at 1438

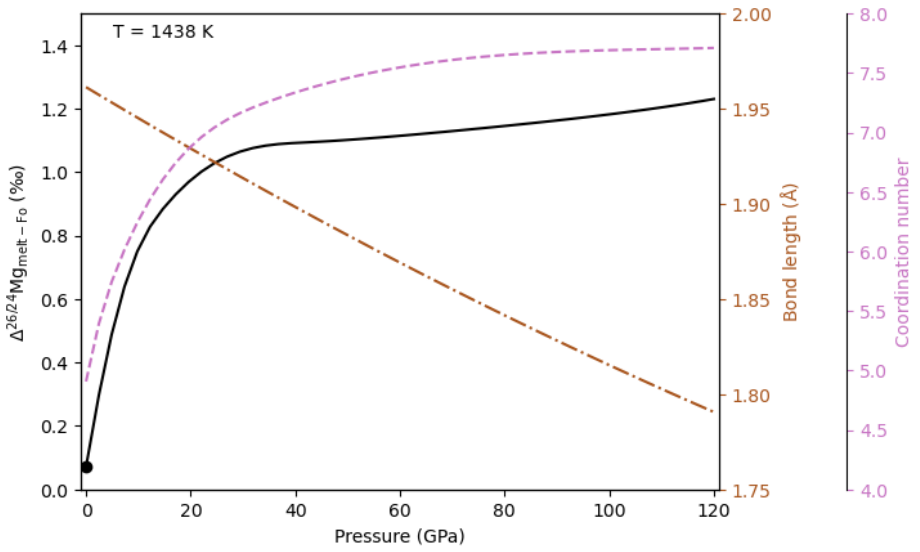

Figure 7: Predicted fractionation between liquid Mg_2SiO_4 and Fo as a function of pressure (black, left axis) from an ionic model based on melt structure data from de Koker et al. (2009) pinned to the observed fractionation between forsterite and melt at ambient pressure (black dot). Bond lengths are parameterised by a polynomial (brown, inner right axis) and coordination numbers by piecewise cubic splines (mauve, outer right axis).

K, as qualitatively expected from the higher coordination number of Mg in olivine compared to low pressure silicate melt. There is currently no empirical evidence that variation in (ultra-)mafic silicate liquid composition affects isotopic fractionation but given the increasing coordination number of Mg in silicate liquid, we cannot assume that $^{26}Mg/^{24}Mg$ ratios in (ultra-)mafic silicate liquid remain constant to lower mantle pressures. Instead, we build an 'ionic' model following the approach of Young et al. (2015) but making modifications to fit the DFT results presented above. This class of models assume the vibrational behaviour of Mg atoms can be described by an effective Born–Mayer type interatomic potential:

$$E(r) = \frac{z_1 z_2}{r}\left(\frac{e^2}{4\pi\epsilon_0}\right) + \frac{b}{r^n}, \tag{6}$$

which gives the bonding energy, E, as a function of the mean distance between Mg and O ions, r. The first term in Equation 6 represents Coulomb interactions and the second represents repulsion due to the overlap of electron clouds. Balancing these terms gives an equilibrium bond length, r_0, which minimises E. The parameters z_1 and z_2 represent the charges on the ions, e is the charge of an electron, and ϵ_0 is the vacuum permittivity. The parameters b and n define the strength and shape of the repulsion term.

In the ionic model, the vibrational properties and thus isotopic fractionation are determined from the effective force constant K_f, which is the second derivative of Equation 6 evaluated at r_0:

$$K_f = \left.\frac{\mathrm{d}^2 E}{\mathrm{d}r^2}\right|_{r=r_0} = \frac{z_1 z_2 e^2 (1-n)}{4\pi\epsilon_0 r_0^3}, \tag{7}$$

with n treated as an adjustable parameter (commonly set to 12), formal charges assumed, and where b is written in terms of the equilibrium bond

length ($b = -\left(e^2/4\pi\epsilon_0\right) z_1 z_2 / n r_0^{n-1}$) and eliminated. This allows calculation of the reduced partition function:

$$\beta = 1 + \frac{1}{24}\left(\frac{h}{k_B T}\right)^2 \frac{K_f}{4\pi^2}\left(\frac{1}{m} - \frac{1}{m'}\right), \tag{8}$$

We find that no single value of n or choice of ionicity, ζ, to scale the charges (i.e. $z_1 = \zeta \times 2.0$ and $z_2 = \zeta \times -2.0$), gives a good fit to the results presented in Figure 4, even for a single coordination number. We therefore choose to extend the model by making ζ a function of equilibrium bond length and coordination number, n_c, allowing a model with three adjustable parameters: $\zeta = \zeta_0 + r_0\zeta_r + n_c\zeta_c$. We fit these parameters to the calculated reduced fractionation factors for all hypothetical MgO polymorphs at 300 K fixing n at 12. The resulting model is shown by the dotted lines in Figure 4. As well as fitting the DFT calculations, this prescription gives reasonable effective potentials and effective charges (Figure 8).

This ionic model allows us to use the combination of empirical low pressure measurement fractionation between olivine and coexisting melt at low pressure together with the pressure evolution of the average structure of silicate melts to calculate the reduced partition function for Mg in the melt phase. To do this, we use the data of de Koker et al. (2009), shown in Figure 7, to find the bond length and coordination number in the melt at the pressure of interest, evaluate the effective force constant using the model shown in Figure 4, and then use Equation 8 to compute the reduced partition function for the melt at the temperature of interest. In order to ensure consistency with the empirical result for fractionation between melt and olivine we apply a constant offset (of 7.8 GPa) to the the pressure scale in Figure 7. The resulting predicted fractionation along a chondritic liquidus is shown

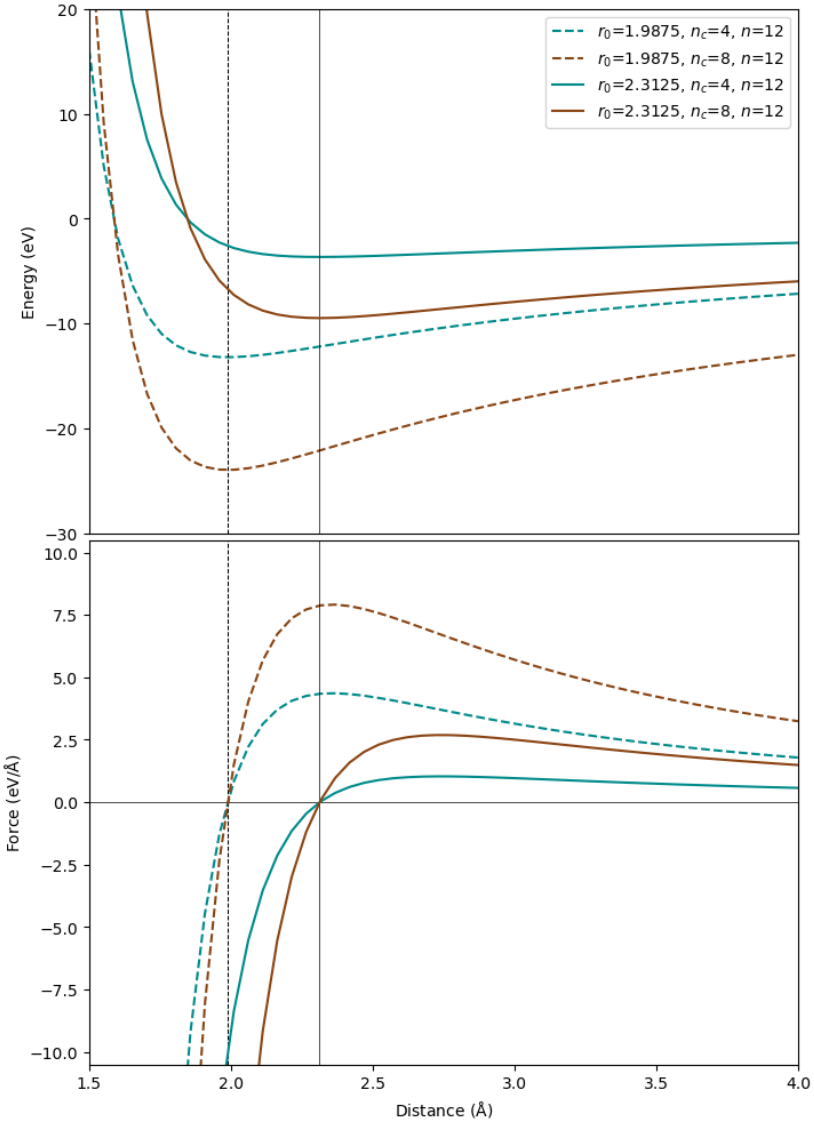

Figure 8: Energy and force from effective interatomic potentials for equilibrium bond lengths of 1.9875 and 2.3125 Å and coordination numbers of 4.0 and 8.0. All models have $n = 12$. These models are represented by the small filled and unfilled circles in Figure 4. ζ for these extreme models varies between 0.95 ($n_c = 8$ and $r_0 = 1.9875$) and 0.40 ($n_c = 4$ and $r_0 = 2.3125$).

in Figure 9 taking the melt as the reference phase. The rapid increase in the mean Mg coordination number in the melt as pressure increases from 0 to 25 GPa results in a rapid decrease in $\Delta^{26/24}$Mg between the liquid and coexisting solids. This trend then reverses as the coordination number of the melt stops increasing and the bond compressibility in the melt dominates the modelled fractionation. Because the bond lengths in the melt decrease in length more slowly than the bond lengths in the solids (as added flexibility means the melt can decrease volume without a reduction in bond length) $\Delta^{26/24}$Mg between the liquid and coexisting solids begins to increase but remains more extreme than the ambient pressure value. This trend continues throughout the mantle pressure range. In principle these patterns should impart an isotopic signature on the crystallising mantle that could persist to today.

Depth	Pressure	Temperature	$1000\ln(\beta)$			
(km)	(GPa)	(K)	Fo	Bdm	MgO	melt
1000	39	3136	0.388	0.278	0.332	0.653
1500	62	3691	0.353	0.247	0.297	0.553
2000	87	4204	0.314	0.222	0.261	0.488
2500	113	4692	0.250	0.189	0.203	0.442

Table 6: Summary fractionation factors along a chondritic liquidus. Solids from DFPT with thermal expansion, liquid from an ionic model pinned to the empirical measurement at ambient pressure

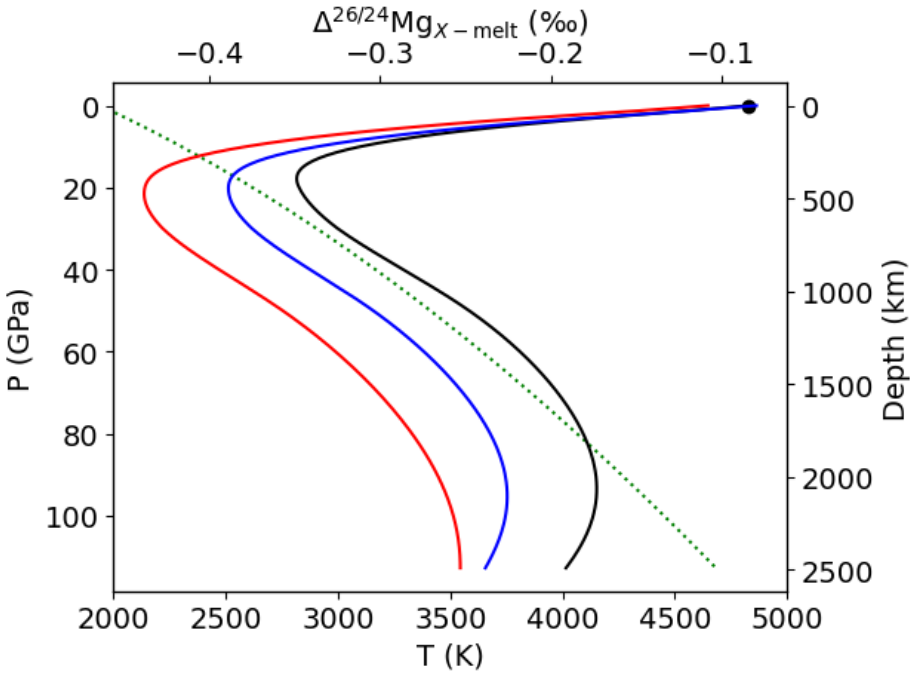

Figure 9: Calculated equilibrium partitioning (top axis) between forsterite (black lines), bridgmanite (red lines) or periclase (blue lines) and melt as a function of depth along a chondritic liquidus. The black dot shows the observed fractionation between forsterite and melt to which the model curves are pinned. The green doted line relates depth to pressure (left axis) and temperature (bottom axis) for the chondritic liquidus.

4.2. Implications for global magma oceans

In the aftermath of a giant, moon-forming impact the Earth's mantle was largely molten (Benz and Cameron, 1990; Tonks and Melosh, 1993). From either bottom-up (e.g. Solomatov and Stevenson, 1993) or middle-out crystallisation scenarios (Labrosse et al., 2007), bridgmanite would be expected to be the dominant crystallising phase (e.g. Ito et al., 2004). If any bridgmanite cumulate reservoirs were preserved, they would have a significant impact on trace and even major element abundances of the accessible mantle (e.g. Kato et al., 1988). However, vigorous convection in both magma ocean and the subsequently crystallised mantle acts against such a reservoir persisting through Earth history (e.g. Solomatov and Stevenson, 1993). Nonetheless, numerous studies still invoke the chemical consequences of a primordial planetary magma ocean in shaping modern mantle compositions (see discussion in Walter and Trønnes, 2004). The significant Mg isotopic fractionation between bridgmanite and melt that we have quantified for lower mantle pressures provides a useful means to test some of these scenarios.

As a moderately refractory element, the Mg isotopic compositions of chondritic meteorites give a valuable estimate of bulk Earth and in turn bulk silicate Earth, given Mg is highly lithophile and minimally incorporated into the core. Recent, critical mixture double spiking analyses have helped refine the composition of chondrites (Hin et al., 2017) and the accessible upper mantle (Liu et al., 2023). These new data show that the Earth's accessible mantle is slightly isotopically heavier than the likely dominant chondritic starting materials by some 12-38 ppm in $\Delta^{26/24}$Mg, assuming enstatite chondrite type protolith based on its isotopic similarity to Earth (Dauphas, 2017). Although

the difference in $\Delta^{26/24}$Mg between (enstatite) chondrite and Earth was previously explained by evaporative loss during accretion (Hin et al., 2017), the sense of fractionation is also compatible with loss of bridgmanite from the accessible mantle composition, a concept which has been the focus of some renewed attention (see review in Murakami et al., 2024). Here we explore this latter possibility more quantitatively using our new fractionation factors.

We consider a simple batch model of magma ocean crystallisation, as it has been argued that the vigour of convective mixing in the magma ocean makes fractional removal of solid phases unlikely until at least 50% crystallisation (Solomatov and Stevenson, 1993). The consequences of increasing amounts of solid bridgmanite removal from a global magma ocean are illustrated on Figure 10. Loss of isotopically light bridgmanite from the magma ocean increases the ^{26}Mg/^{24}Mg of the residual melt (red lines, Figure 10) relative to its initial, chondritic composition. If some proportion of the crystallised bridgmanite remains isolated through Earth history, due it its higher viscosity for example (Ballmer et al., 2017), then the convectively stirred, accessible mantle will acquire the Mg isotopic composition of the (subsequently crystallised) evolved liquid shown in Figure 10.

We use fractionation factors for ^{26}Mg/^{24}Mg between bridgmanite and melt at two different depths: at 2500 km appropriate for crystallisation at the base of a magma ocean and at 1000 km to represent mid-mantle crystallisation (Caracas et al., 2019). These two values should span the range of crystallisation scenarios and the outcomes are shown as solid and dashed lines respectively in Figure 10. We assume pure bridgmanite fractionation, which is likely the case for up to 50% crystallisation of the magma ocean, although

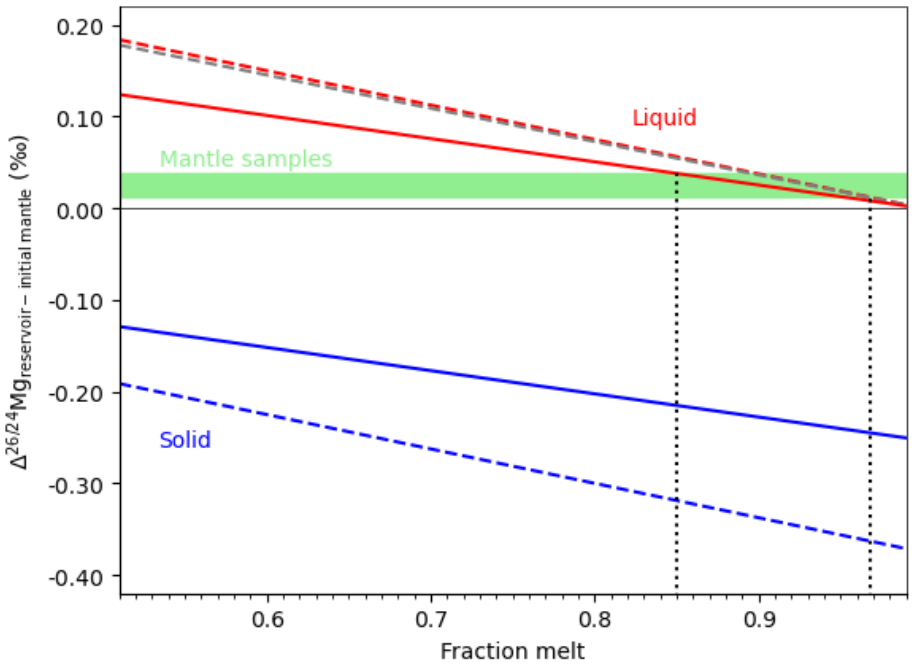

Figure 10: Difference in $^{26}Mg/^{24}Mg$ relative to an initial (chondritic) composition ($\Delta^{26/24}Mg$, expressed in ‰) of evolving melt (red lines) and solid (blue lines) during magma ocean crystallisation. We consider the first 50% crystallisation (i.e. melt fraction, by mass, decreases from 1 to 0.5) in which interval crystallisation is likely a batch process (Solomatov and Stevenson, 1993) and bridgmanite the dominant crystallising phase (Ito et al., 2004). The effect of also including 10 wt.% ferropericlase fractionation with the bridgmanite has a minor effect (shown as grey dashed line compared to red dashed line). Scenarios using two different fractionation factors from Table 6 are shown: the solid lines for deep mantle crystallisation (2500 km) and dashed lines for mid mantle crystallisation (1000 km). The green box indicates the range of composition of the samples from the Earth's mantle (Liu et al., 2023) relative to an enstatite chondrite starting composition (Hin et al., 2017). Depending on the fractionation scenario, 3-15 wt.% bridgmanite fractionation (and subsequent isolation, indicated by the vertical black dotted lines) is sufficient to explain the super-chondritic $^{26}Mg/^{24}Mg$ of the Earth's mantle.

590 the additional contribution of ferropericlase to the crystallisation assemblage,
591 which is also isotopically light relative to melt in the lower mantle (Table 6),
592 does not significantly change the calculations (Figure 10).

593 The differences in Mg isotope compositions between terrestrial mantle
594 samples and enstatite chondrites (isotopically the most similar chondrite
595 group to Earth) are shown as a green box on Figure 10. In order to re-
596 produce these $\Delta^{26/24}$Mg requires a minimum of 3 wt.% and maximum of
597 15 wt.% bridgmanite crystallisation and its subsequent convective isolation.
598 This range of bridgmanite fractionation is similar to that suggested by Walter
599 and Trønnes (2004) as being compatible with a range of refractory element
600 ratios in silicate Earth. We note that the latter estimates also require minor
601 davemaoite crystallisation to counter-act some the more extreme trace ele-
602 ment fractionations of bridgmanite on key trace element ratios, whereas our
603 estimate is not sensitive to this additional consideration. The amount of con-
604 vectively isolated bridgmanite required to satisfy the Mg isotope constraints
605 is also consistent with the geodynamical simulations of Gülcher et al. (2020).

606 While these calculations might suggest a hidden, cumulate bridgmanite
607 reservoir is a plausible solution to the accessible Earth having superchondritic
608 mantle ^{26}Mg/^{24}Mg, the longevity of stiff, bridgmanite domains in the mantle
609 still needs to be fully explored in 3-dimensional simulations. Moreover there
610 are additional considerations from mass dependent Si isotope measurements.
611 The Moon and accessible terrestrial mantle are indistinguishable in their
612 $\Delta^{30/28}$Si (Fitoussi and Bourdon, 2012; Zambardi et al., 2013; Armytage et al.,
613 2011). Fitoussi and Bourdon (2012) argued that this left little scope for a
614 hidden bridgmanite reservoir on Earth, given bridgmanite is also anticipated

to fractionate Si as well as Mg isotopes at magma ocean conditions (Huang et al., 2014). Given our progress in providing melt-bridgmanite fractionation factors, extending this approach to Si, to couple with new critically mixed double spike measurements (Liu et al., 2024), would be valuable to address this issue in new detail.

5. Conclusions

We have made ab initio calculations of Mg isotope fractionation between the major Mg-bearing phases of the lower mantle from the transition zone (25 GPa) to core mantle boundary (120 GPa). For temperatures on a chondritic liquidus (3200-4700 K), and including the effects of thermal expansion, fractionations of $^{26}Mg/^{24}Mg$ between a fictive Fo reference and Per and Bdm vary from 0.056-0.047‰ and 0.11-0.061‰, respectively. Thus, we reconfirm that diminished isotopic fractionation resulting from higher temperatures deeper in the Earth are sufficiently compensated by the effects of pressure to permit discernible Mg isotopic fractionations under lower mantle conditions.

We have also made an initial estimate of the isotopic fractionation between the solid lower mantle phases and co-existing melt. We first calculated the $1000\ln\beta$ for a set of MgO-structured minerals with different Mg coordination number and Mg-O bond length, to allow us to parameterise the effects of these two controls on isotopic fractionation. We then used data from ab initio models of melt structure to characterise Mg coordination and Mg-O bond length in silicate melts with changing pressure. The model was then pinned to an empirical determination of $^{26}Mg/^{24}Mg$ fractionation between forsterite and melt at 0 GPa. Using this approach, we predict $\Delta^{26/24}Mg_{Melt-Bdm}$ 0.38-

0.23‰ from the transition zone to core mantle boundary for temperatures on a chondritic liquidus. Using this quantification of the influence of melt structure on Mg isotopic fractionation we show that the highly coordinated Mg site in Bdm leads to discernible Mg isotopic fractionation during its crystallisation from a magma ocean.

Using these fractionation factors in combination with $^{26}Mg/^{24}Mg$ measurements made to a precision of <20 ppm can provide useful constraints on scenarios of magma ocean crystallisation. This approach rules out hidden, primordial cumulate reservoirs greater than 20 wt.% of the mantle but suggests that the slightly super-chondritic $^{26}Mg/^{24}Mg$ of the Earth could be explained by removal of 3-15% Bdm during magma ocean crystallisation, if primordial cumulate bridgmnaite can be retained, unmixed with the rest of the mantle over Earth history, as hypothesised in the BEAMS concept of Ballmer et al. (2017). The strength of this explanation relative to a previous proposal of evaporative loss (Hin et al., 2017) could usefully be tested with a similar quantification of deep mantle Si isotope fractionation.

Acknowledgments

We acknowledge the use of HECToR, ARCHER and ARCHER2 the UK's national high-performance computing services. We thank the two anonymous reviewers of a 2014 version of this manuscript who provided some useful suggestions. This work is supported by grants from NERC (NE/L007428/1 and NE/K008803/1) and the ERC (NONUNE, 885531).

Data Availability

Density functional theory calculations were performed using the CASTEP code with code available via https://www.castep.org/. Input and output files for these calculations are available through Zenodo at https://doi.org/10.5281/zenodo.16760721. Software used to calculate and fit reduced partition functions, and create all figures presented in this manuscript, is also available through Zenodo at https://doi.org/10.5281/zenodo.16744738.

Appendix A. Supplementary Material

The supplementary file describes our parametrisation of reduced partition functions for crystals and melt with pressure, temperature and depth. It also includes tables of the fitted coefficients used for this alongside an expanded version of Table 6.

References

Andrault, D., Bolfan-Casanova, N., Lo Nigro, G., Bouhifd, M.A., 2011. Solidus and liquidus profiles of chondritic mantle: Implication for melting of the earth across its history. Earth and Planetary Science Letters 304, 251 – 259. doi:10.1016/j.epsl.2011.02.006.

Armytage, R.M.G., Georg, R.B., Savage, P.S., Williams, H.M., Halliday, A.N., 2011. Silicon isotopes in meteorites and planetary core formation. Geochimica et Cosmochimica Acta 75, 3662 – 3676. doi:10.1016/j.gca.2011.03.044.

Ballmer, M.D., Houser, C., Hernlund, J.W., Wentzcovitch, R.M., Hirose, K., 2017. Persistence of strong silica-enriched domains in the Earth's lower mantle. Nature Geoscience 10, 236–240. doi:10.1038/ngeo2898.

Baroni, S., Ginnozzi, P., Testa, A., 1987. Green's-function approach to linear response in solids. Physical Review Letters 58, 1861 – 1864.

Baroni, S., de Gironcoli, S., Corso, A.D., Giannozzi, P., 2001. Phonons and related crystal properties from density-functional perturbation theory. Reviews of Modern Physics 73, 515 – 562.

Benz, W., Cameron, A.G.W., 1990. Terrestrial Effects Of The Giant Impact, in: Origin of the Earth. Oxford University PressNew York, NY, pp. 61–67. URL: https://academic.oup.com/book/53843/chapter/422184126, doi:10.1093/oso/9780195066197.003.0005.

Bigeleisen, J., Mayer, M.G., 1947. Calculation of equilibrium constants for isotopic exchange reactions. Journal of Chemical Physics 15, 261 – 267. doi:10.1063/1.1746492.

Blanchard, M., Balan, E., Schauble, E.A., 2017. Equilibrium fractionation of non-traditional isotopes: a molecular modeling perspective. Reviews in Mineralogy and Geochemistry 82, 27–63. doi:10.2138/rmg.2017.82.2.

Blanchard, M., Poitrasson, F., Méheut, M., Lazzeri, M., Mauri, F., Balan, E., 2009. Iron isotope fractionation between pyrite (FeS_2), hematite (Fe_2O_3) and siderite ($FeCO_3$): A first-principles density functional theory study. Geochimica et Cosmochimica Acta 73, 6565 – 6578.

Caracas, R., Hirose, K., Nomura, R., Ballmer, M.J., 2019. Melt–crystal density crossover in a deep magma ocean. Earth and Planetary Science Letters 516, 202–211. doi:10.1016/j.epsl.2019.03.031.

Clark, S.J., Segall, M.D., Pickard, C.J., Hasnip, P.J., Probert, M.I.J., Refson, K., Payne, M.C., 2005. First principles methods using CASTEP. Zeitschrift fuer Kristallographie 220, 567 – 570.

Dauphas, N., 2017. The isotopic nature of the earth's accreting material through time. Nature 541, 521–524. doi:10.1038/nature20830.

Duan, H., Yang, B., Huang, F., 2023. Site-specific isotope effect: Insights from equilibrium magnesium isotope fractionation in mantle minerals. Geochimica et Cosmochimica Acta 357, 13–25. doi:10.1016/j.gca.2023.05.015.

Fitoussi, C., Bourdon, B., 2012. Silicon isotope evidence against an enstatite chondrite Earth. Science 335, 1477 – 1480. doi:10.1126/science.1219509.

Gao, C., Cao, X., Liu, Q., Yang, Y., Zhang, S., He, Y., Tang, M., Liu, Y., 2018. Theoretical calculation of equilibrium mg isotope fractionations between minerals and aqueous solutions. Chemical Geology 488, 62–75. doi:10.1016/j.chemgeo.2018.04.005.

Giannozzi, P., de Gironcoli, S., Pavone, P., Baroni, S., 1991. *Ab initio* calculation of phonon dispersion in semiconductors. Physical Review B 43, 7231 – 7242.

Gonze, X., 1997. First-principles responses of solids to atomic displacements

and homogeneous electric fields: Implementation of a conjugate-gradient algorithm. Physical Review B 55, 10337 – 10354.

Gonze, X., Lee, C., 1997. Dynamical matrices, Born effective charges, dielectric permittivity tensors, and interatomic force constants from density-functional perturbation theory. Physical Review B 55, 10355 – 10368.

Gülcher, A.J.P., Gebhardt, D.J., Ballmer, M.J., Tackley, P.J., 2020. Variable dynamic styles of primordial heterogeneity preservation in the earth's lower mantle. Earth and Planetary Science Letters 536, 116160. doi:10.1016/j.epsl.2020.116160.

Hin, R.C., Coath, C.D., Carter, P.J., Nimmo, F., Lai, Y.J., Pogge Von Strandmann, P.A.E., Willbold, M., Leinhardt, Z.M., Walter, M.J., Elliott, T., 2017. Magnesium isotope evidence that accretional vapour loss shapes planetary compositions. Nature 549, 511–515. doi:10.1038/nature23899.

Hohenberg, P., Kohn, W., 1964. Inhomogeneous electron gas. Physical Review 136, 864 – 871.

Huang, F., Chen, L., Wu, Z., Wang, W., 2013. First-principles calculations of equilibrium Mg isotope fractionations between garnet, clinopyroxene, orthopyroxene, and olivine: Implications for Mg isotope thermometry. Earth and Planetary Science Letters 367, 61 – 70. doi:10.1016/j.epsl.2013.02.025.

Huang, F., Wu, Z., Huang, S., Wu, F., 2014. First-principles calculations of equilibrium silicon isotope fractionation among mantle minerals. Geochimica et Cosmochimica Acta 140, 509 – 520. doi:10.1016/j.gca.2014.05.035.

Ito, E., Kubo, A., Katsura, T., Walker, M.J., 2004. Melting experiments of mantle materials under lower mantle conditions with implications for magma ocean differentiation. Physics of the Earth and Planetary Interiors 143-144, 397–406. doi:10.1016/j.pepi.2003.09.016.

Javoy, M., Balan, E., Méheut, M., Blanchard, M., Lazzeri, M., 2012. First-principles investigation of equilibrium isotopic fractionation of O- and Si-isotopes between refractory solids and gases in the solar nebula. Earth and Planetary Science Letters 319-320, 118 – 127. doi:10.1016/j.epsl.2011.12.029.

Karki, B.B., Bhattarai, D., Stixrude, L., 2006. First-principles calculations of the structural, dynamical, and electronic properties of liquid MgO. Physical Review B 73, art. num. 174208. doi:10.1103/PhysRevB.73.174208.

Kato, T., Ringwood, A.E., Irifune, T., 1988. Experimental determination of element partitioning between silicate perovskites, garnets and liquids: constraints on early differentiation of the mantle. Earth and Planetary Science Letters 89, 123–145. doi:10.1016/0012-821x(88)90038-6.

Keiffer, S.W., 1982. Thermodynamics and lattice vibrations of minerals: 5. applications to phase equilibria, isotopic fractionation, and high-pressure thermodynamic properties. Reviews of Geophysics and Space Physics 20, 827 – 849.

Kohn, W., Sham, L.J., 1965. Self-consistent equations including exchange and correlation effects. Physical Review 140, 1133 – 1138.

de Koker, N., 2009. Thermal conductivity of MgO periclase from equilibrium first principles molecular dynamics. Physical Review Letters 103, 125902. doi:10.1103/PhysRevLett.103.125902.

de Koker, N.P., Stixrude, L., Karki, B.B., 2009. Thermodynamics, structure, dynamics, and freezing of Mg_2SiO_4 liquid at high pressure. Geochimica et Cosmochimica Acta 72, 1427 – 1441.

Kowalski, P.M., Jahn, S., 2011. Prediction of equilibrium Li isotope fractionation between minerals and aqueous solutions at high P and T: An efficient *ab initio* approach. Geochimica et Cosmochimica Acta 75, 6112 – 6123. doi:10.1016/j.gca.2011.07.039.

Kowalski, P.M., Wunder, B., Jahn, S., 2013. *Ab initio* prediction of equilibrium boron isotope fractionation between minerals and aqueous fluids at high P and T. Geochimica et Cosmochimica Acta 101, 285 – 301. doi:dx.doi.org/10.1016/j.gca.2012.10.007.

Labrosse, S., Hernlund, J.W., Coltice, N., 2007. A crystallizing dense magma ocean at the base of the Earth's mantle. Nature 450, 866 – 869. doi:10.1038/nature06355.

Li, X., Liu, Y., 2011. Equilibrium Se isotope fractionation parameters: A first-principles study. Earth and Planetary Science Letters 304, 113 – 120. doi:10.1016/j.epsl.2011.01.022.

Li, X., Zho, H., Tang, M., Liu, Y., 2009. Theoretical prediction for several important equilibrium Ge isotope fractionation factors and geolog-

ical implications. Earth and Planetary Science Letters 287, 1 – 11. doi:10.1016/j.epsl.2009.07.027.

Liu, X.N., Hin, R., Coath, C., van Soest, M., Melekhova, E., Elliott, T., 2022. Equilibrium olivine-melt Mg isotopic fractionation explains high δ^{26}Mg values in arc lavas. Geochemical Perspectives Letters 22, 42–47. doi:10.7185/geochemlet.2226.

Liu, X.N., Hin, R.C., Coath, C.D., Bizimis, M., Su, L., Ionov, D.A., Brooker, R., Elliott, T., 2023. The magnesium isotopic composition of the mantle. Geochimica et Cosmochimica Acta 358, 12–26. doi:10.1016/j.gca.2023.08.011.

Liu, X.N., Klava, M., Hin, R.C., Coath, C.D., Ng, H.C., Elliott, T., 2024. High-precision, mass dependent si isotope measurements *via* the critical mixture double-spiking technique. Journal of Analytical Atomic Spectrometry 39, 2799–2808. doi:10.1039/d4ja00152d.

Méheut, M., Lazzeri, M., Balan, E., Mauri, F., 2007. Equilibrium isotopic fractionation in the kaolinite, quartz, water system: Prediction from first-principles density-functional theory. Geochimica et Cosmochimica Acta 71, 3170 – 3181. doi:10.1016/j.gca.2007.04.012.

Méheut, M., Lazzeri, M., Balan, E., Mauri, F., 2009. Structural control over equilibrium silicon and oxygen isotopic fractionation: A first-principles density-functional theory study. Chemical Geology 258, 28 – 37. doi:10.1016/j.chemgeo.2008.06.051.

Monkhorst, H.J., Pack, J.D., 1976. Special points for Brillouin-zone integrations. Physical Review B 13, 5188 – 5192.

Mookherjee, M., Stixrude, L., Karki, B., 2008. Hydrous silicate melt at high pressure. Nature 452, 983 – 986.

Murakami, M., Kahn, A., Sossi, P.A., Ballmer, M.D., Saha, P., 2024. The composition of Earth's lower mantle. Annual Review of Earth and Planetary Sciences 52, 605–638. doi:10.1146/annurev-earth-031621-075657.

Payne, M.C., Teter, M.P., Allan, D.C., Arias, T., Joannopoulos, J.D., 1992. Iterative minimization techniques for *ab initio* total-energy calculations: molecular-dynamics and conjugate gradients. Reviews of Modern Physics 64, 1045 – 1067.

Perdew, J.P., Burke, K., Emzerhof, M., 1996. Generalized gradient approximation made simple. Physical Review Letters 77, 3865 – 3868.

Rabin, S., Blanchard, M., Pinilla, C., Poitrasson, F., Grégoire, M., 2023. Iron and silicon isotope fractionation in silicate melts using first-principles molecular dynamics. Geochimica et Cosmochimica Acta 343, 212–233. doi:10.1016/j.gca.2022.11.017.

Refson, K., Tulip, P.R., Clark, S.J., 2006. Variational density-functional perturbation theory for dielectrics and lattice dynamics. Physical Review B 73, 155114. doi:10.1103/PhysRevB.73.155114.

Rustad, J.R., Bylaska, E.J., 2006. Ab initio calculation of isotopic fractionation in $B(OH)_3$(aq) and BOH_4^-(aq). Journal of the American Chemical Society (communications) 129, 2222 – 2223.

Rustad, J.R., Dixon, D.A., 2009. Prediction of iron-isotope fractionation between hematite (α-Fe_2O_3) and ferric and ferrous iron in aqueous solution from density functional theory. Journal of Physical Chemistry A 113, 12249 – 12255. doi:10.1021/jp9065373.

Schauble, E.A., 2004. Applying stable isotope fractionation theory to new systems. Reviews in Mineralogy and Geochemistry 55, 65 – 111.

Schauble, E.A., 2011. First-principles estimates of equilibrium magnesium isotope fractionation in silicate, oxide, carbonate and hexaaquamagnesium(2+) crystals. Geochimica et Cosmochimica Acta 75, 844 – 869. doi:10.1016/j.gca.2010.09.044.

Soderman, C.R., Shorttle, O., Matthews, S., M., W.H., 2022. Global trends in novel stable isotopes in basalts: Theory and observations. Geochimica et Cosmochimica Acta 318, 388–414. doi:10.1016/j.gca.2021.12.008.

Solomatov, V.S., Stevenson, D.J., 1993. Nonfractional crystallization of a terrestrial magma ocean. Journal of Geophysical Research 98, 5391 – 5406.

Sossi, P.A., O'Neill, H.St.C., 2017. The effect of bonding environment on iron isotope fractionation between minerals at high temperature. Geochimica et Cosmochimica Acta 196, 121–143. doi:10.1016/j.gca.2016.09.017.

Stixrude, L., Karki, B.B., 2005. Structure and freezing of $MgSiO_3$ liquid in Earth's lower mantle. Science 310, 297 – 299. doi:10.1126/science.1116952.

Sun, N., Stixrude, L., de Koker, N., Karki, B.B., 2011. First principles molecular dynamics simulations of diopside ($CaMgSi_2O_6$) liquid to high pressure. Geochimica et Cosmochimica Acta 75, 3792 – 3802.

Teng, F.Z., Wadhwa, M., Helz, R.T., 2007. Investigation of magnesium isotope fractionation during basalt differentiation: implications for a chondritic composition of the terrestrial mantle. Earth and Planetary Science Letters 261, 84 – 92.

Tonks, W.B., Melosh, H.J., 1993. Magma ocean formation due to giant impacts. Journal of Geophysical Research 98, 5319 – 5333. doi:10.1029/92JE02726.

Urey, H.C., 1947. The thermodynamic properties of isotopic substances. Journal of the Chemical Society , 562 – 581doi:10.1039/JR9470000562.

Walter, M.J., Trønnes, R.G., 2004. Early Earth differentiation. Earth and Planetary Science Letters 225, 253–269. doi:10.1016/j.epsl.2004.07.008.

Wang, W., Tian, Q., Chen, Z., Huang, S., Wu, Z., Huang, F., 2017. Concentration effect on equilibrium fractionation of Mg-Ca isotopes in carbonate minerals: Insights from first-principles calculations. Geochimica et Cosmochimica Acta 208, 185–197. doi:10.1016/j.gca.2017.03.023.

Wang, W., Wu, Z., Huang, S., Huang, F., 2023. First-principles investigation of equilibrium magnesium isotope fractionation among mantle minerals: Review and new data. Earth-Science Reviews 237, 104315. doi:10.1016/j.earscirev.2023.104315.

Wang, W., Zhou, C., Liu, Y., Wu, Z., Huang, F., 2019. Equilibrium Mg isotope fractionation among aqueous Mg^{2+}, carbonates, brucite and lizardite: Insights from first-principles molecular dynamics simulations. Geochimica et Cosmochimica Acta 250, 117–129. doi:10.1016/j.gca.2019.01.042.

Wentzcovitch, R.M., Yu, Y.G., Wu, Z., 2010. Thermodynamic properties and phase relations in mantle minerals investigated by first principles quasiharmonic theory, in: Wentzcovitch, R.M., Stixrude, L. (Eds.), Theoretical and computational methods in mineral physics: geophysical applications. Mineralogical society of America and the Geochemical Society. volume 71 of *Reviews in Mineralogy and Geochemistry*. chapter 4, pp. 59 – 98.

Wu, Z., Huang, F., Huang, S., 2015. Isotope fractionation induced by phase transformation: First-principles investigation for Mg_2SiO_4. Earth and Planetary Science Letters 409, 339 – 347. doi:10.1016/j.epsl.2014.11.004.

Xiao, Z.C., Zhou, C., Kang, J.T., Z.-Q., W., Huang, F., 2022. The factors controlling equilibrium inter-mineral ca isotope fractionation: Insights from first-principles calculations. Geochimica et Cosmochimica Acta 333, 373–389. doi:10.1016/j.gca.2022.07.021.

Yagi, T., Mao, H.K., Bell, P.M., 1978. Structure and crystal chemistry of perovskite-type $MgSiO_3$. Physics and Chemistry of Minerals 3, 97 – 110. doi:10.1007/BF00308114.

Young, E.D., Manning, C.E., Schauble, E.A., Shahar, A., Macris, C.A., 2015. High-temperature equilibrium isotope fractionation of non-traditional stable isotopes: Experiments, theory, and applications. Chemical Geology 395, 176 – 195. doi:10.1016/j.chemgeo.2014.12.013.

Young, E.D., Tonui, E., Manning, C.E., Schauble, E., Macris, C.A., 2009. Spinel–olivine magnesium isotope thermometry in the mantle and impli-

cations for the Mg isotopic composition of Earth. Earth and Planetary Science Letters 288, 524 – 533. doi:10.1016/j.epsl.2009.10.014.

Zambardi, T., Poitrasson, F., Corgne, A., Méheut, M., Quitté, G., Anand, M., 2013. Silicon isotope variations in the inner solar system: Implications for planetary formation, differentiation and composition. Geochimica et Cosmochimica Acta 121, 67–83. doi:10.1016/j.gca.2013.06.040.

Supplementary information for: Controls on Mg isotopic fractionation between deep mantle phases and relict signatures of a terrestrial magma ocean

Andrew M. Walker

Department of Earth Sciences, University of Oxford, South Parks Road, Oxford, OX1 3AN, UK.

Remco C. Hin

Institute of Environmental Geology and Geoengineering, Conaiglio Nazionale delle Ricerche, Via Bianco Mario 9, 20131, Milano MI, Italy.

Tim Elliott

School of Earth Sciences, University of Bristol, Queen's Road, Bristol, BS8 1RT, UK.

1 Parametrisation of magnesium fractionation in crystals as a function of depth

In Figure 6 in the main text we present results of the fractionation of magnesium isotopes between forsterite and MgO, and forsterite and bridgmanite as a function of depth along a geotherm for two cases. In the first (shown with dashed lines) we neglect the thermal expansion of the three phases. The parametrisation for this case is fairly compact and given by Equation 5 and Table 3 in the main text. The second cases (shown as a solid line in Figure 6) includes the differential thermal expansion of the phases as calculated using lattice dynamics in the quasi-harmonic approximation. While probably more accurate, the parametrisation for this case demands many more terms. Here we outline the steps we use to generate the data in Figure 6, and list the full set of parameters to allow our results to be reused.

It is first worth noting that we are interested in calculating the isotopic fractionation along the chondritic melting curve of Andrault et al. (2011) which, for any depth, defines the temperature, T, and pressure, P, where we will evaluate the fractionation. However, the reduced partition functions are calculated as a function of unit cell volume, V, and

T. The first stage is thus to find V for the relevant P and T. To do this, we first calculate the Helmholtz free energy, F, as a function of T for unit cells of fixed structure and hence fixed V. The structures are found by static minimisation of the enthalpy for 16 applied pressures between −10 and 140 GPa in 10 GPa increments. Results for each T are fit to isothermal third-order Birch-Murnaghan equations of state:

$$F(V) = F_0 + \frac{9V_0K_0}{16}\left\{\left[\left(\frac{V_0}{V}\right)^{\frac{2}{3}} - 1\right]^3 K_0' + \left[\left(\frac{V_0}{V}\right)^{\frac{2}{3}} - 1\right]^2 \left[6 - 4\left(\frac{V_0}{V}\right)^{\frac{2}{3}}\right]\right\}. \quad (1)$$

In order to find the volume at any temperature and pressure, we fit the four parameters, X, of these equations (the zero pressure Helmholtz free energy, F_0, the zero pressure volume, V_0, the zero pressure bulk modulus, K_0, and its pressure derivative K_0') to fifth order polynomials in T:

$$X(T) = X_5T^5 + X_4T^4 + X_3T^3 + X_2T^2 + X_1T + X_0, \quad (2)$$

and this allows us to easily find the parameters for any temperature, which allows us to evaluate the pressure as a function of volume at that temperature from the derivative of Equation 1:

$$P(V) = \frac{3K_0}{2}\left[\left(\frac{V_0}{V}\right)^{\frac{7}{3}} - \left(\frac{V_0}{V}\right)^{\frac{5}{3}}\right]\left\{1 + \frac{3}{4}(K_0' - 4)\left[\left(\frac{V_0}{V}\right)^{\frac{2}{3}} - 1\right]\right\}. \quad (3)$$

Coefficients of Equation 2 are given in Table 1. The results are also shown in Figure 5 of the main text. Equation 3 is not invertible, so to find volume as a function of pressure we resort to a numerical approach and perform a bisection search (using SciPy; Virtanen et al., 2020) to find the volume for which Equation 3 returns the desired pressure (for parameters which depend on temperature using Equation 2).

The reduced partition functions are similarly calculated as a function of unit cell volume and temperature for the same set of cell volumes. To allow interpolation to other temperatures or cell volumes these results are fit to the function:

$$\begin{aligned} 1000\ln\left(\beta(V,T)\right) = &\left(A_1 + A_2V^{-1}\right)T^{-6} \\ &+ \left(B_1 + B_2V^{-1} + B_3V^{-2}\right)T^{-4} \\ &+ \left(C_1 + C_2V^{-1} + C_3V^{-2}\right)T^{-2}, \end{aligned} \quad (4)$$

with values of the eight coefficients given in Table 2.

X		Fo	Per	Bdm
F_0	X_0 (eV)	-7.87×10^{3}	-1.99×10^{3}	-5.88×10^{3}
	X_1 (eV/K)	1.09×10^{-3}	4.00×10^{-4}	9.78×10^{-4}
	X_2 (eV/K^2)	-1.04×10^{-5}	-3.17×10^{-6}	-7.17×10^{-6}
	X_3 (eV/K^3)	3.38×10^{-9}	1.06×10^{-9}	2.27×10^{-9}
	X_4 (eV/K^4)	-6.92×10^{-13}	-2.21×10^{-13}	-4.55×10^{-13}
	X_5 (eV/K^5)	5.80×10^{-17}	1.88×10^{-17}	3.78×10^{-17}
V_0	X_0 (Å^3)	3.03×10^{2}	77.9	1.70×10^{2}
	X_1 (Å^3/K)	3.03×10^{-3}	6.86×10^{-4}	8.78×10^{-4}
	X_2 (Å^3/K^2)	1.07×10^{-5}	3.29×10^{-6}	5.94×10^{-6}
	X_3 (Å^3/K^3)	-4.87×10^{-9}	-1.55×10^{-9}	-2.86×10^{-9}
	X_4 (Å^3/K^4)	1.23×10^{-12}	3.99×10^{-13}	7.36×10^{-13}
	X_5 (Å^3/K^5)	-1.01×10^{-16}	-3.46×10^{-17}	-6.77×10^{-17}
K_0	X_0 (GPa)	1.19×10^{2}	1.48×10^{2}	2.27×10^{2}
	X_1 (GPa/K)	-1.02×10^{-2}	-1.08×10^{-2}	-1.26×10^{-2}
	X_2 (GPa/K^2)	-1.23×10^{-5}	-1.84×10^{-5}	-2.48×10^{-5}
	X_3 (GPa/K^3)	6.81×10^{-9}	1.03×10^{-8}	1.39×10^{-8}
	X_4 (GPa/K^4)	-1.78×10^{-12}	-2.68×10^{-12}	-3.62×10^{-12}
	X_5 (GPa/K^5)	1.74×10^{-16}	2.61×10^{-16}	3.52×10^{-16}
K_0'	X_0	4.07	4.20	3.96
	X_1 (K^{-1})	1.32×10^{-4}	1.15×10^{-4}	1.23×10^{-4}
	X_2 (K^{-2})	-6.59×10^{-9}	2.00×10^{-8}	-3.98×10^{-9}
	X_3 (K^{-3})	1.10×10^{-11}	-5.86×10^{-12}	1.96×10^{-14}
	X_4 (K^{-4})	-2.73×10^{-15}	1.53×10^{-15}	8.12×10^{-16}
	X_5 (K^{-5})	3.79×10^{-19}	-4.84×10^{-20}	-1.01×10^{-19}

Table 1: Polynomial coefficients used to parametrise the temperature dependence of the isothermal third-order Birch-Murnaghan equation of state for each phase.

	Fo	Per	Bdm
A_1 (K^6)	-8.3811×10^{15}	-6.3595×10^{15}	-6.9939×10^{15}
A_2 (K^{6}Å^3)	2.4239×10^{18}	4.7423×10^{17}	1.1706×10^{18}
B_1 (K^4)	-2.3070×10^{11}	-2.8718×10^{11}	-3.4351×10^{11}
B_2 (K^{4}Å^3)	1.6240×10^{14}	4.8439×10^{13}	1.2732×10^{14}
B_3 (K^{4}Å^6)	-2.9121×10^{16}	-2.1005×10^{15}	-1.2127×10^{16}
C_1 (K^2)	1.5128×10^{6}	2.8116×10^{6}	4.2687×10^{6}
C_2 (K^{2}Å^3)	-7.1553×10^{8}	-6.0676×10^{8}	-1.9792×10^{9}
C_3 (K^{2}Å^6)	4.4884×10^{11}	4.4657×10^{10}	2.7596×10^{11}

Table 2: Coefficients of Equation 4, used to find the reduced partition functions at chosen temperatures and cell volumes.

2 Parametrisation of magnesium fractionation in silicate liquid as a function of depth

As described in the main text, we parametrise the reduced partition function in the melt by fitting an ionic model to a range of results from hypothetical oxides in terms of bond length and coordination number as shown in Figure 4. In this approach, the reduced partition function is given by Equation 8 in the main text with the effective force constant given by Equation 7. We fix the parameter n at 12, set $z_2 = -z_1$, and we find the best fit when:

$$z_1 = (2.32716768 - 0.93910997 r_0 + 0.06109785 n_c) \times 2.0, \tag{5}$$

where the coordination number, n_c, and bond length r_0, vary with hypothetical oxide and applied pressure. We assume the same parametrisation can be applied to the melt structure of de Koker et al. (2009) and presented in their Figure 7. We note that temperature has limited impact on coordination number and bond length and we neglect the effect of temperature on these aspects of the melt structure. We describe the evolution of bond length (in Å) with pressure (in GPa) according to the polynomial:

$$r_0 = 1.9613P - 0.00165P^2 + 0.0000019P^3 \tag{6}$$

and describe the evolution of coordination number with pressure using interpolating splines given the data points in Table 3. This parametrisation allows us to estimate the reduced partition function for melt as a function of pressure and temperature (which is included via Equation 8 of the main text). The effect of pressure on coordination number, bond length and reduced partition function of the melt is illustrated in Figure 7 of the main text.

P (GPa)	n_c	P (GPa)	n_c
0.1	4.93	34.3	7.25
2.5	5.40	72.1	7.62
7.2	6.00	159.4	7.85
16.3	6.70		

Table 3: Mg coordination number in melt at selected pressures from de Koker et al. (2009).

The approaches outlined above allow the calculation of β at any chosen pressure and temperature for Per, Bdm, Fo and melt and from this we can calculate the expected isotopic fractionation using Equation 1 in the main text. This approach is used to construct Figures 6 and 9, and Table 6 in the main text. We provide an expanded version of Table 6 below (Table 4) and make the code used to perform these calculations available (see Walker, 2025).

Depth (km)	Pressure (GPa)	Temperature (K)	$1000\ln(\beta)$ Fo	Bdm	Per	melt
14.1	0.3	1953.3	0.486	0.459	0.489	0.587
98.5	2.9	2052.8	0.477	0.431	0.466	0.689
182.9	5.7	2154.3	0.467	0.406	0.446	0.756
267.3	8.6	2254.5	0.458	0.385	0.429	0.789
351.8	11.6	2354.3	0.449	0.366	0.413	0.797
436.2	14.7	2454.9	0.440	0.350	0.399	0.788
520.6	17.9	2557.1	0.431	0.336	0.386	0.773
605.0	21.3	2658.4	0.423	0.323	0.375	0.756
689.4	24.8	2761.0	0.415	0.311	0.364	0.736
773.9	28.6	2865.6	0.407	0.301	0.354	0.713
858.3	32.3	2968.1	0.399	0.292	0.345	0.690
942.7	36.1	3068.7	0.392	0.283	0.337	0.668
1027.1	40.0	3167.4	0.385	0.276	0.330	0.646
1111.6	43.9	3264.4	0.379	0.270	0.323	0.626
1196.0	47.8	3359.7	0.373	0.264	0.317	0.607
1280.4	51.8	3453.5	0.367	0.259	0.311	0.591
1364.8	55.8	3545.8	0.362	0.254	0.305	0.575
1449.2	59.8	3636.8	0.356	0.249	0.300	0.561
1533.7	63.9	3726.6	0.350	0.245	0.295	0.547
1618.1	68.0	3815.2	0.345	0.241	0.289	0.535
1702.5	72.1	3902.7	0.339	0.237	0.284	0.523
1786.9	76.3	3989.2	0.333	0.233	0.278	0.512
1871.4	80.5	4074.9	0.326	0.228	0.272	0.502
1955.8	84.8	4159.7	0.319	0.224	0.265	0.493
2040.2	89.0	4243.7	0.310	0.220	0.258	0.483
2124.6	93.4	4327.1	0.302	0.215	0.249	0.475
2209.0	97.8	4409.9	0.292	0.210	0.240	0.467
2293.5	102.2	4492.2	0.281	0.204	0.230	0.459
2377.9	106.7	4574.2	0.269	0.198	0.220	0.452
2462.3	111.2	4655.8	0.256	0.192	0.208	0.445
2546.7	115.8	4737.2	0.242	0.185	0.196	0.438
2631.2	120.5	4818.5	0.228	0.178	0.184	0.432
2715.6	125.2	4899.9	0.213	0.171	0.171	0.426

Table 4: Additional fractionation factors along a chondritic liquidus. Solids from DFPT with thermal expansion, liquid from an ionic model pinned to the empirical measurement at ambient pressure. See Table 4 of the main text.

References

D. Andrault, N. Bolfan-Casanova, G. Lo Nigro, and M. A. Bouhifd. Solidus and liquidus profiles of chondritic mantle: Implication for melting of the earth across its history. *Earth and Planetary Science Letters*, 304:251 – 259, 2011. doi: 10.1016/j.epsl.2011.02.006.

N. P. de Koker, L. Stixrude, and B. B. Karki. Thermodynamics, structure, dynamics, and freezing of Mg_2SiO_4 liquid at high pressure. *Geochimica et Cosmochimica Acta*, 72:1427 – 1441, 2009.

P. Virtanen, R. Gommers, T. E. Oliphant, M. Haberland, T. Reddy, D. Cournapeau, E. Burovski, P. Peterson, W. Weckesser, J. Bright, S. J. van der Walt, M. Brett, J. Wilson, K. J. Millman, N. Mayorov, A. R. J. Nelson, E. Jones, R. Kern, E. Larson, C. J. Carey, İ. Polat, Y. Feng, E. W. Moore, J. VanderPlas, D. Laxalde, J. Perktold, R. Cimrman, I. Henriksen, E. A. Quintero, C. R. Harris, A. M. Archibald, A. H. Ribeiro, F. Pedregosa, P. van Mulbregt, and SciPy 1.0 Contributors. SciPy 1.0: Fundamental Algorithms for Scientific Computing in Python. *Nature Methods*, 17:261–272, 2020. doi: 10.1038/s41592-019-0686-2.

A. Walker. andreww/isofrac: Version 0.1.0. Zenodo, 2025. URL https://doi.org/10.5281/zenodo.16744739.